Heliyon 8 (2022) e09525

Contents lists available at ScienceDirect

Heliyon

journal homepage: www.cell.com/heliyon

Research article

Structural interpretation of Southern Main Ethiopian Rift basin using constrained full tensor gravity inversion of the basement morphology

Bisrat Kebede [a,b,*], Tilahun Mammo [a], Abebe Misgie [c]

[a] School of Earth Science, Addis Ababa University, P.O. Box 1176, Addis Ababa, Ethiopia
[b] Ministry of Mines and Petroleum, P.O. Box 486, Addis Ababa, Ethiopia
[c] Geological Survey of Ethiopia, P.O. Box 40069, Addis Ababa, Ethiopia

ARTICLE INFO

Keywords:
Basement
Inversion
Density
Structures
Sub-basin
Modeling

ABSTRACT

The Southern Main Ethiopian Rift is part of the great East African Rift system situated within the limit of 37°–38.5° east and 5.5°–7° north. Unlike the Central and Northern Main Ethiopian Rift where numerous geophysical studies have been conducted, the subsurface geology of Southern Main Ethiopian Rift is poorly constrained. Geological field work on Amaro Horst shows the basement outcrops are dominated by High grade gneisses and Intrusive with an average density of 6 gm/cm^3 overlain by Mesozoic sedimentary rocks possibly extend into the studied sub-basins. In addition, field structural measurements and extracted lineaments from digital elevation model show NE–SW, NW–SE and N–S directions in agreement with fault block geometries identified by Invariance Tensor analysis. The Precambrian basement morphology of the area is delineated using constrained Tensor Gravity Inversion by applying Parker–Oldenburg algorisms. The basement morphology depicts the sub-basins; Northern Abaya, Southern Abaya, Chamo and Gelana basins where these areas are characterized by low Bouguer anomaly below -175mGal and lower Invariance Tensor anomaly may show the sediment infill of the sub-basins. The deepest depression exceeds 2500m below sea level in northern Abaya sub-basin where the maximum sediment thickness is more than 3700m. The result agrees with Spectral and Euler source depths solutions that show the limits of the crystalline basement vary between 2500m and 3500m. Amaro Horst, Chencha and Agere Selam are the basement structural high with average sediment thickness of 500m. The basement morphology revealed the N–S orientation of Gelana basin and other sub-basins aligns with NE–SW Tertiary Rifting. This result agrees with the structural analysis as well as previous regional studies on directions of prominent geological structures. These structurally controlled sub-basins having thick sedimentary sections are favorable zones for follow-up hydrocarbon exploration.

1. Introduction

The Main Ethiopian Rift (MER) which is part of the East African Rift system (EARS) where extensional deformation or rifting began as early as late Oligocene-early Miocene times (Bellahsen et al., 2003; Ebinger et al., 2000; Ghebreab, 1998; Morley et al., 1992). The MER rift is composed of three main segments; northern, central, and southern MER in which the divisions of these segments are marked by E-W trending transverse structures, the Goba-Bonga lineament separating the central MER from the southern MER (Abbate and Sagri, 1980) and the Yerer-Tullu Wellel volcanotectonic lineament (YTVL) is a boundary between the northern and the central MER (Abebe et al., 1998). Gravity surveys can be utilized at a wide range of scales, ranging from regional tectonic studies and sub-regional hydrocarbon and mineral exploration surveys to local engineering and environmental problems (Corwin and Ward, 1990; Hinze, 1990; Paterson and Reeves, 1985). In a geophysical prospecting inversion of gravity anomalies is an important techniques for determining the geometry of the Moho and crystalline basement density interface depth (Feng et al., 2015). Density interfaces are closely associated with the boundaries of geological structures which provides vital information in understanding deep structures, regional tectonics and basin architecture, there are many kinds of methods proposed by different authors involved in potential field inversion (R J Blakely, 1995; Gubbins, 2004; Menke, 2018; Zhdanov, 2002). Using gravity anomalies, many approaches have been applied to determine the nature of the undulations of the Basement and Moho depths (Cordell and Henderson, 1968; Rao and Babu, 1991), in

* Corresponding author.
E-mail addresses: kbisrat79@gmail.com, kbisrat50@yahoo.com (B. Kebede).

https://doi.org/10.1016/j.heliyon.2022.e09525
Received 14 October 2021; Received in revised form 1 February 2022; Accepted 18 May 2022

which the total gravity anomalies are calculated as the sum of all rectangular prisms of constant density. Another approach to delineate the basement relief is through Global Optimization (Ekinci et al., 2021), a stochastic derivative-free vector-based metaheuristic named differential evolution algorithm (DEA). The most widely used methods of inverting the depth of a density interface using potential field anomalies is the Parker–Oldenburg approach, that is, Parker (1973) made the forward calculation of a potential field where as Oldenburg (1974) rearranging it to determine the density interface.

Since there are very few previous geophysical studies in the area, the subsurface structures of Southern MER are poorly known unlike the Central and Northern MER which are well constrained with geophysical studies. This paper aimed to determine the subsurface geometry of the basement morphology using constrained gravity and gravity gradient anomalies inversion based on the Parker–Oldenburg algorithm in order to determine the structures, architectures and associated sediment thickness of the southern MER basin essentially to assess the hydrocarbon potential of the area.

The commonly discussed Bouguer anomaly and the vertical gravity gradient (G_{zz}) component is sufficient to produce geologically reasonable and interpretable results, while including additional components of horizontal derivatives G_{xx}, G_{xy}, G_{yy}, G_{xz}, G_{yz} and G_{yz} increases the resolution of the recovered geometry of the basement morphology. The gravity gradients correlate better than gravity with geological features such as rifts, fold belts, edges, linear structures and magmatic deposits and intrusions and are an ideal tool to follow geological units associated with the basement relief below a stratigraphic layer of varying sediments density (Braitenberg et al., 2011). In the absences of constrains in which performing inversion is difficult, depth estimations of the sediment infill of the basin is very crucial step, such results are used to produce best estimate initial depth to source that can act as initial models for any detailed quantitative modeling exercises using 2D/3D forward/inverse modeling techniques. Thus Euler Depth solutions and Spectral depth estimations performed in this study, depth estimations using Tilt Angle (Kebede and Mammo, 2021) and EAGLE controlled source wide-angle reflection/refraction 2D seismic velocity models (Maguire et al., 2006), geology and nearby well data (Tullow Oil, 2014) have been used as a prior or axillary information's. To better understand the geology of the area and to obtain optimal value of basement density, geological field works were conducted. During field work structural measurements are carried out and over 30 Precambrian basement and other rock samples are collected and analyzed. DEM based extracted lineaments and structures deduced from Invariance of Tensor Gravity fields are also integrated with the final results of the structural inversion.

2. Overviews of the geology

The Tertiary rift system of Ethiopia can be divided into three main areas: the Southern Rift Basins, the Main Ethiopian Rift (MER) and Afar (Figure 1). An attempt has been made to classify the basins according to their plate tectonic setting and the combination of plate tectonics and geodynamics became powerful one to understand the origin and development of sedimentary basins (Ingersoll, 1988; Klein, 1990; Klemme, 1980; Miall, 1995; Tucker, 2009). Major oil discoveries onshore on Uganda and Kenya tertiary rift trigger the explorations of oil and gas in MER (Purcell, 1981). Drilling have shown thick sediments and oil-prone Paleogene lacustrine source rocks in Southern Ethiopian Rift basins (Purcell, 2007), and similar rocks are present near Jimma in the Ethiopian rift basins (Wolela, 2006), these source rocks could generate significant volumes of oil and gas if buried to sufficient depth. Miocene lacustrine shales are known in the Main Ethiopian Rift and Afar, and Paleogene equivalents can reasonably be expected in the subsurface and higher heat flow and burial under the thick Tertiary basalts could have matured the source rocks, with oil migrating into interbedded or juxtaposed reservoirs (Purcell, 2007). On the other hand the pervasive volcanism and the high geothermal regime will have a possibility of destroyed any hydrocarbons generated in these rifts (Purcell, 2007). Subsurface temperatures measured in the MER from geothermal wells reveals thermal levels destructive to hydrocarbons, 320 °C at 2200 m at Aluto/Langanno and 270 °C at 2100 m at Tendaho, however, these high temperatures concentrated along magmatic segments and should not be generalized over the entire rift (Purcell, 2007). Exposed sections of pre-Tertiary sediments-Mesozoic sediments are observed (sandstone and limestone units of the Adigrat and Antalo Formations, respectively, along with shale and marl beds) resting unconformably on the crystalline basement, typical examples of such occurrences is at Kella horst, Guraghe area, along the western margin at the Escarpment (WoldeGabriel and Aronson, 1986) and in the Amaro Horst of the southern sector of the MER (Levitte et al., 1974; Mohr, 1962; Mohr and Gouin, 1967; Zanettin et al., 1978) and it is infered that considerable thicknesses of sediment fill sections exist in these segmented rift grabens. In continental area petroleum system is associated with narrow rifts, within which two new petroleum provinces have been established this century in the Albertine and South Lokichar Basins (Macgregor et al., 2018). Since there is no significant exploration for oil and gas deposits in the Main Ethiopian Rift, there is very little information on the subsurface stratigraphy or structure in these basins and it is not known if an effective Tertiary petroleum system is present.

3. Methods

3.1. Geological field work

Field study shows that the study area is underlain by Precambrian basement rocks, Cenozoic volcanic rocks, Quaternary and pre Tertiary sediment. Since the main objective of the geological field work is to collect Precambrian basement rock samples for density determinations to better constrain the 3D-structural inversions, and the primary targeted area were selected on the bases of previous geological studies (Mengesha et al., 1996). Thus most of the samples are collected on Amaro horst and few samples are collected on southeastern part of Lake Chamo to Konso and on western plateau (Kemba) where basement outcrops are dominant.

During field work structural measurements are also carried out, with the Strike and Dip directions presented in (Table 1). Intrusive rock, pre-rift sediment (red Sandston), Cenozoic volcanic rocks and Quaternary sediments were observed in the southern MER where more than 30 Precambrian basements and other rock samples are collected along five traverses of total length 945km (Figure 2).

Water Absorption, Porosity and bulk density determinations were carried out by the Geological Survey of Ethiopia Mineralogy and Geotechnical Laboratory Directorate (Table 1).

Constraints from geological field work are utilized for the definition of outcrops of metamorphic basement rock layers and determination of average density values (~2.6 gm/cm^3) to accommodate lateral variations of basement rock density in the study area (Table 1). Amaro Horst is used as a control point, the only reliable basement tie for the study area which is a narrow block of Precambrian basement caped with thick tertiary basalt with highest elevation more than 3200 m above sea level separating Chamo basin to the west and Galana basin to the east widens and declines southwards over a length of ~90 km (Ebinger et al., 1993; Levitte et al., 1974).

3.1.1. High grade gneisses

(i) Gneiss; during field activities high grade gneiss compositionally hornblende biotite gneiss (Figure 3a) and Quartz Feldspar gneiss (Figure 3b) are observed, this unit exposed around Northern parts of Amaro Horst at Kele, it is medium to coarse grained light grey and black in color interlayered between Quaritzo feldspatic gneiss and biotite hornblende gneiss previously mapped as hornblende gneiss. This unit is also exposed on western plateau of Kemba area; it is highly weathered and changed to sand. ***(ii) Migmatite rocks;*** this unit exposed southwest of study area along konso road on the river bed. The Migmatite gneiss

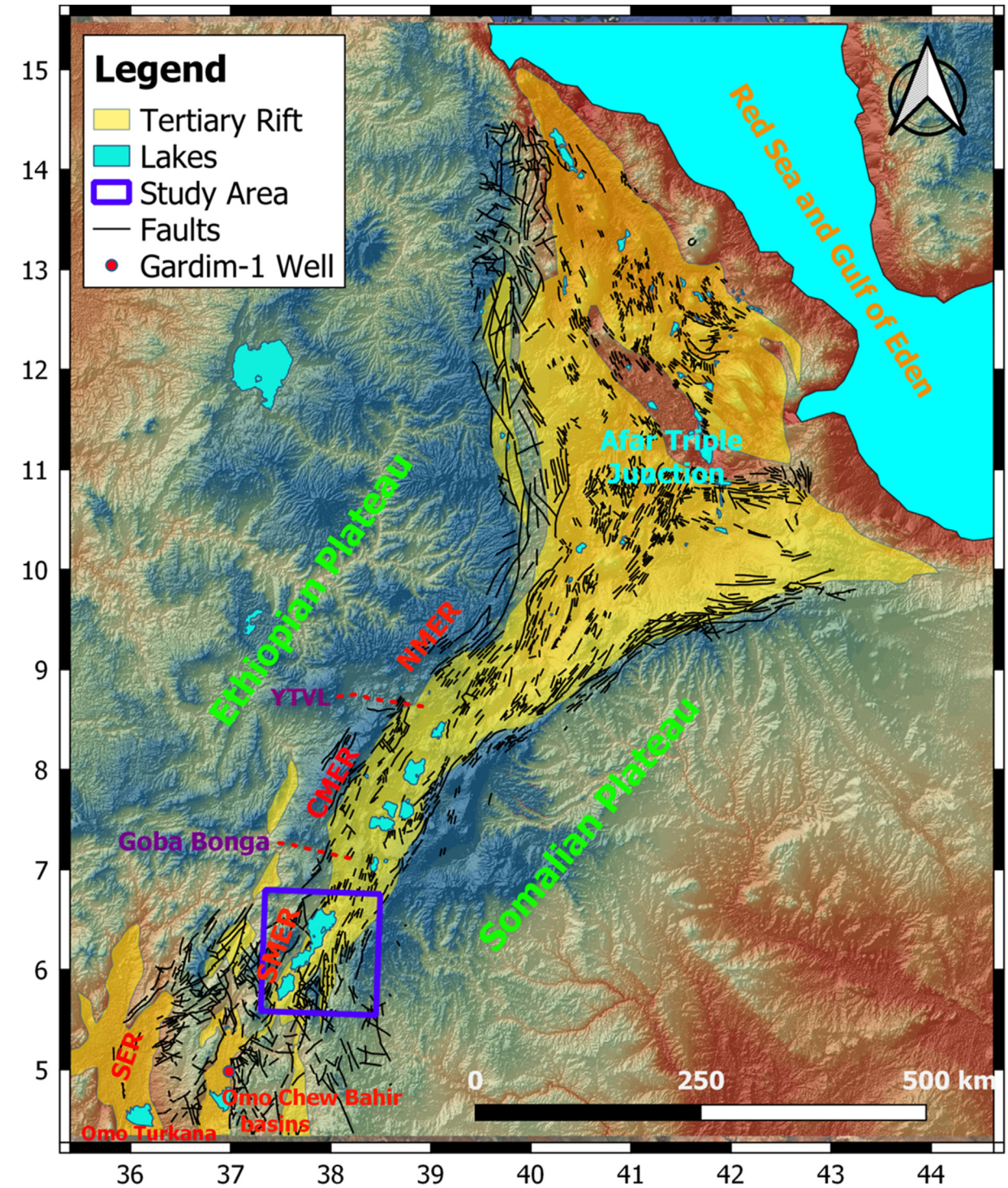

Figure 1. Ethiopian Tertiary Rift system, SRTM digital elevation model, Faults extracted from geological map of Ethiopia (Mengesha et al., 1996).

(Figure 3c) is dark grey; medium to coarse grained and strongly layered. Interlayered with this rock are fine to medium and coarse grained, dark biotite dominated and light feldspar dominated layers. Compositional banding is largely migmatitic and parallels internal foliation which is strongly deformed. ***(iii) Mafic Gneiss;*** the unit also found at the southwest corner of the study area near Gato town. Mafic Gneiss (Figure 3d) is characterized by a layering of amphibolite, mafic hornblende gneiss and relatively lighter colored (leucocratic) gneiss. Amphibolite and less mafic hornblende gneiss are interlayered in various ratios and at different scale within most of this unit. ***(iv) Granitoid Gneiss (Granite Gneiss);*** the unit exposed in stream cut exposure and the rock compositionally Quartz and feldspar (granitic) but it is highly metamorphosed. Light grey color medium grained slightly weathered similar to Quartizo feldspatic gneiss the difference is weathering and mineral banding.

3.1.2. *Intrusive rocks*

(i) Metagranite; the unit is exposed in the Northwest of the study area near Soyoma Town. It is characterized exfoliation weathering and foliated, coarse grained light grey in color rig forming topography. ***(ii) Granodiorite;*** The unit exposure northwest of Ager Mariam town shows porphyritic granodiorite which is a strongly variable rock, locally having a distinctly porphyritic fabric with coarse euhedral K-feldspar

Table 1. Water Absorption, Porosity and bulk density determinations of sampled rocks by Geological Survey of Ethiopia Mineralogy and Geotechnical Laboratory Directorate: H.W= Highly Weathered. T = Traverse, S=Station, R = Rock and B=Basement.

ID.No	Rock Name	Water Absorption %	Porosity %	Bulk Density gm/cm^3	Strike	Dip
T1S1RB-001	Quartzite gneiss	0.86	2.21	2.55	210	86
T1S2RB-002	Quartzite gneiss	3.12	8.14	2.60	310	35
T1S3RB-003	Basalt	2.00	5.59	2.78	205	70
T1S4RB-004	Quartzite and Biotite gneiss	4.05	10.91	2.69	10	32
T1S5RB-005	Aphanetic basalt	1.19	3.40	2.85	135	35
T2S6RB-006	Feldspatic gneiss	1.39	3.59	2.56	144	88
T2S7RB-007	Basalt	0.67	1.96	2.90	194	65
T2S8RB-008	Quartzite gneiss	1.78	4.56	2.54	203	80
T2S9RB-009	Basalt	0.84	2.42	2.85	198	86
T2S10RB-010	Metagranite	1.02	2.67	2.59	205	84
T2S11RB-011	Metagranite	1.44	3.75	2.58	192	86
T2S12RB-012	Granodiorite	0.74	2.03	2.72	170	65
T3S13RB-013	Metagranite	1.11	2.83	2.53	225	45
T3S14RB-014	Red sandstone	-	-	-	-	-
T3S15RB-015	Granit gneiss	1.94	4.37	2.62	320	75
T3S16RB-016	Basalt	2.46	6.64	2.68	-	-
T3S17RB-017	Basalt	0.79	2.28	2.86	305	85
T3S18RB-018	Granotoid gneiss	2.09	5.47	2.61	220	70
T3S19RB-019	Megmitite rock	-	-	-	189	45
T4S20RB-020	Quartizofeidspatic gneiss	H.W	H.W	H.W	40	65
T4S21RB-021	Rhyolite	22.26	35.93	1.61	-	-
T4S22RB-022	Basalt	-	-	-	-	-
T5S23RB-023	Basalt	-	-	-	-	-
T5S24RB-024	Basalt	-	-	-	-	-
T5S25RB-025	Basalt	-	-	-	-	-
T5S26RB-026	Gneiss	H.W	H.W	H.W	315	70
T5S27RB-027	Mafic Gneiss	H.W	H.W	H.W	195	48

phenocrysts in a relatively fine-grained matrix. The rock is characterized by augen texture and heterogeneous. The observed Granodiorite Contains many sub-rounded, mafic minerals having gray color and rather fine grained.

3.1.3. Pre-rift sediment

The Precambrian basement rock is overlain unconformably by red Sandstone (Figure 3e). This red sandstone is exposed near Soyoma Town and it is medium to coarse grained which contain basal conglomerate/conglomerate sandstone reddish color and 2 up to 6m thick it is massive and have randomly oriented joint on the surface. Davidson (1983) suggested the red sandstone represented an erosional surface in southwestern Ethiopia and favored a pre Tertiary age for it.

3.1.4. Tertiary volcanic rocks

(i) Lower basalt flows; this is the oldest and most extensive of the volcanic unit in the area. The Lower Basalt (Figure 3f) is characterized by thick, extensive lava flows that locally show columnar jointing in Haro River and highly fractured all the area. It is massive and fine grained. In the northwestern part of the area the tertiary volcanic rock is thick and under lied by rhyolite. WoldeGabriel et al. (1991) uses K/Ar age determinations resulted in the Lower basalt flows dated at 39.8 Ma. ***(ii) Rhyolite flows;*** the rhyolite scamp on the basalt in Chencha but in these areas the rhyolite inter fingered with the basalt and also forms dome. The domes show circular or slightly elliptical in top view. At place the rhyolite made half-domal shaped land form. The rock has fine grained texture, light grey color and commonly shows slickenside.

3.1.5. Quaternary sediments

The quaternary sediment covers Gelana basin and other low land places or the roots of horst. Small amounts of coarse alluvium are found along some of the larger river courses, but the main accumulations are the extensive gravel-sand deposits which form the Gelana flat region to the south of the mapped area. The Gravel-sand and unsorted materials are filling lowlands as part of colluvial and alluvial deposits.

3.2. Mapping lineaments

Investigations of geological structures (Lineaments) play important roles in monitoring of earth quakes and detection of potential zones of oil and gas, minerals and groundwater movements and study of tectonic structure of sedimentary basins (Reddy et al., 2000; Sabins Jr, 1987; Sankar, 2002). Topographic attributes can be extracted from digital elevation data by applying special computer algorithms (Vittala et al., 2006), these include slope, aspect and shaded relief algorithms. Shaded relief derived from digital elevation models is very crucial in identifying lineaments in different distinct relief and topography. DEM has very high resolution than satellite or Landsat images having true projections and tonal variations with no distortion are established or indicated with relief, the position of sun can also be put at different angle at any place above the terrain surface (Batson et al., 1975). Digital Elevation Model have terrain attributes; elevations, curvatures, aspects and slopes which are very crucial for the extractions of structures such as faults and lineaments (Ganas et al., 2005).

High resolution Digital Elevation Model (DEM) 12.5m retrieved from Alaska Satellite Facility's data portal (https://vertex.daac.asf.alaska.edu/) Vertex Alos/Palsar Satellite for remotely sensed imagery of the Earth. Shaded relief image (Figure 4a) was generated from the ALOS PALSAR DEM using a solar azimuth (sun angle) of 45°, and a solar elevation of 30°. Finally, the image has been used for automatic lineaments extraction using PCI Geomatica software 2018 (http://www.pcigeomatics.com/freetrials). PCI Geomatica software algorithm for lineament extraction comprised of curve extraction steps, thresholding and edge detection (Geomatica, 2013). The automated Line tool, a line extraction algorithm within PCI Geomatica was

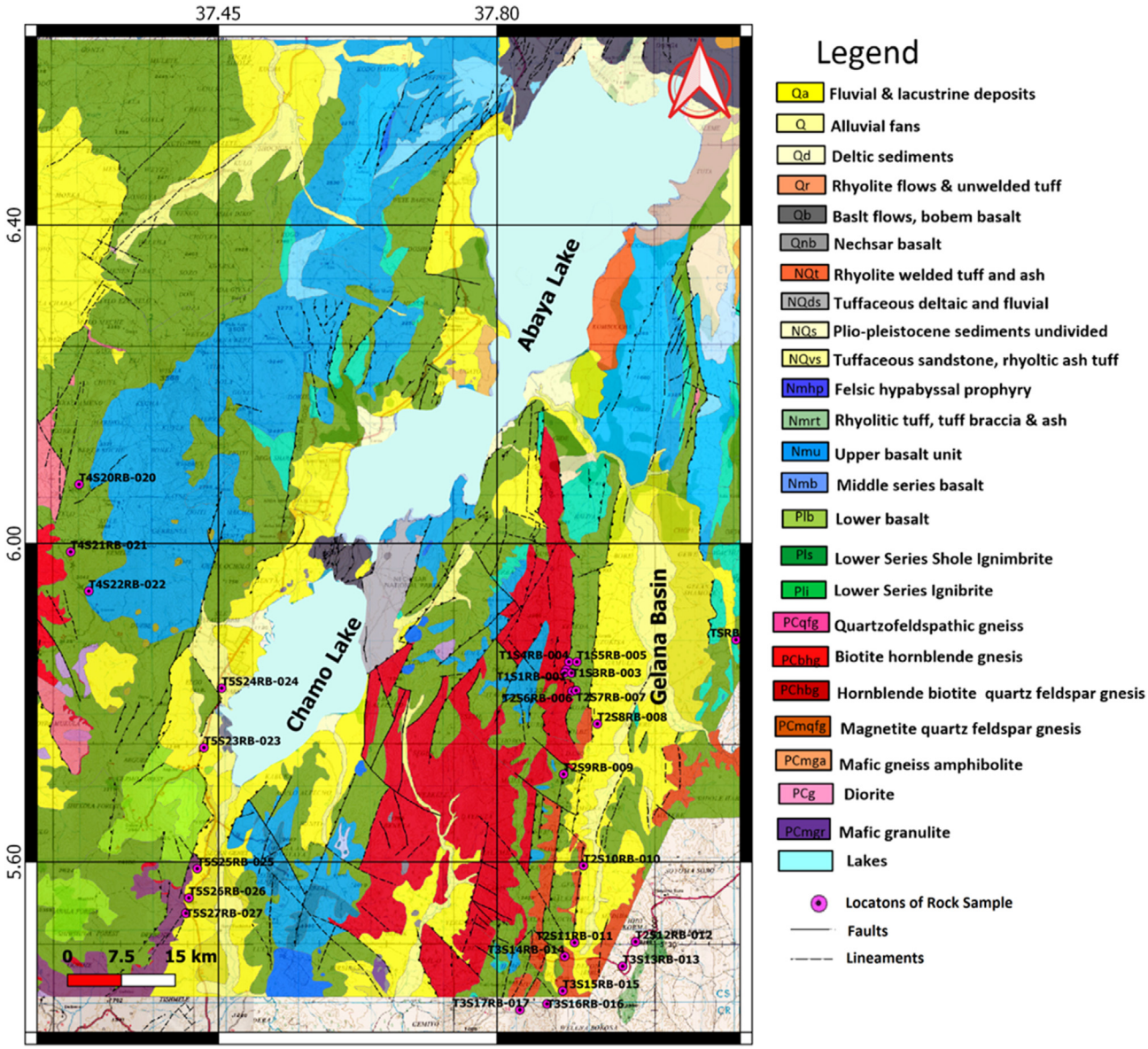

Figure 2. Geological map of the area and Main Ethiopian Rift Stratigraphic column; modified from (AOC and MoM, 2011): the overlaid Yellow points shows Location of field traverse of the rock samples collected.

applied on DEM-derived shaded relief maps using the parameters defined in Table 2 below.

Directional analysis performed on extracted lineaments (Figure 4b) and the orientation of the lineaments represented by the rose diagrams (Figure 4c) shows three prominent trends NE–SW NW–SE and N–S in terms of the length and directional frequency which are indication of the dominant directions of the lineaments. The dominant lineaments tend to run in the NE-SW direction which aligns in the axial portions of the main Ethiopian rift. The measured strike direction (Figure 4c) shows that the dominant direction is NE–SW and NW–SE in agreement with the direction of the extracted lineaments (Figure 4d).

3.3. Full Tensor Gravity

Full Tensor Gravity data is obtained from Ministry of Mines and Petroleum acquired by Africa Oil Ethiopia B.V in main Ethiopian Rift valley basins block. FTGeX Gravity Gradiometry system (Instrument) from Lockheed-Martin used to acquire the Full Tensor Gradiometry (FTG) which include the Gravity Measurement Assembly (GMA) instrument that enable the direct measurement of the vertical gravity signals mounted on a De Havilland Canada DHC6 aircraft (Africa Oil Corp, 2013). The FTG as well as the direct gravity signals were acquired with the main line spacing of 1000 m and Tie line spacing of 5000m designed/flown to follow the terrain at a nominal height of 120m above ground level as shown below (Figure 5). Since Amaro Horst is a Precambrian basement with no hydrocarbon prospect, data was not collected over the entire length of the Horst. Because of the 3D-Structural Inversion does not require any gap in the data, in all steps of data processing and interpretations interpolation is performed.

Full Tensor Gravity Gradiometry (FTG) measures five independent gravity gradients, the horizontal components G_{xx}, G_{xy}, G_{yy}, G_{xz} and G_{yz}, and the vertical components G_{zz} provides a valuable information for the mapping of subsurface geology and tectonic settings of the survey area (Dickinson et al., 2010). While the observed G_{xx} and G_{yy} (Figure 7 a & d) accentuates lineaments and faults in North - South and East - West directions, G_{xz} and G_{yz} (Figure 7 c & e) identify contacts and edges in North - South and East - West directions respectively. The observed vertical gravity gradient G_{zz} (Figure 7f) is equivalent to the observed Bouguer anomaly (Figure 6) except it remove the long wavelengths and preserve intermediate and short wavelengths which is used to estimate depth and

Figure 3. Field photographs of Precambrian basement and other rocks (a) Biotit hornblende gneiss exposed around Northern parts of Amaro Horst at Kele, (b) Quartizo feldspatic gneiss exposed at Western part of the area Kemba Area (c) Migmatite rocks exposed along konso road on the river bed, (d) Mafic gneiss exposed near Gato town (e) Pre-Tertiary rock: Red sandstone exposed near Soyoma Town and (f) Lower Basalt.

predict compositional information related to target geology. Here in a complete Bouguer gravity (g_z) anomaly map of the study area was produced with a grid spacing of 250 m _ 250 m (Figure 6).

The FTG components G_{xx}, G_{xy}, G_{xz}, G_{yz}, G_{yz} and G_{zz} anomaly maps (Figure 7) were produced with the same grid spacing to that of Bouguer gravity (g_z) anomaly map (Figure 6).

3.4. Invariance of Tensor Gravity fields

Full Tensor Gradiometry (FTG) is a high resolution gravity surveying technology that measures different components of the Gravity Gradient Tensor (Murphy, 2004). Since each tensor components of the FTG is part of the same gravity field, treating them as a collective entity is very crucial to obtain valuable information about the subsurface geology. One such method is describe by Pedersen and Rasmussen (1990), the usage of Invariance to compute new tensor representations from Gravity Tensor components. Invariance of Tensor computed using two sets of equations (Eqs. (1) and (2)) that make use of all components simultaneously, those are;

$$I_1 = \sqrt{\left(G_{xx}G_{yy} + G_{yy}G_{zz} + G_{xx}G_{zz}\right) - \left(G_{xy}^2 + G_{yz}^2 + G_{xz}^2\right)} \quad (1)$$

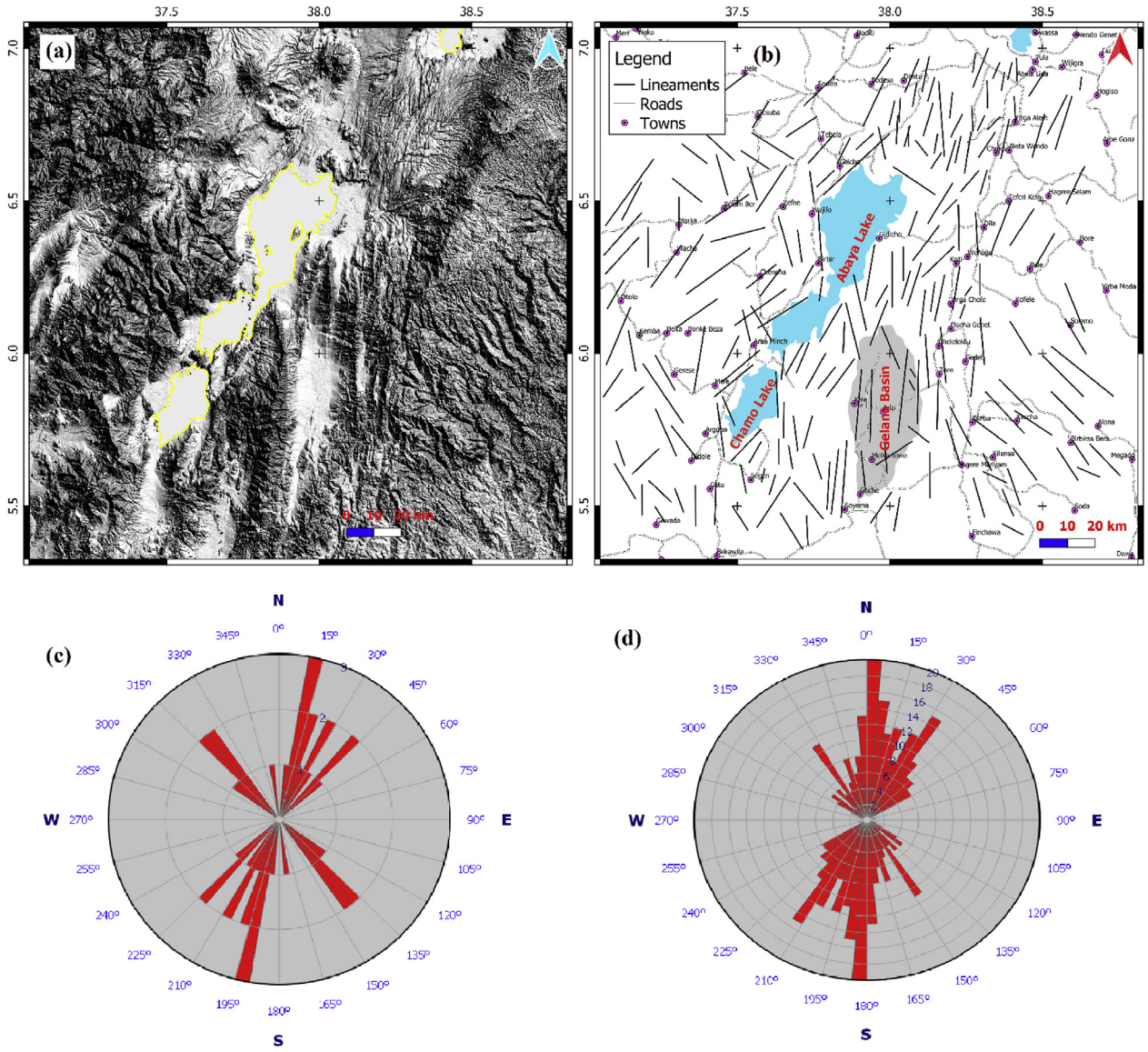

Figure 4. (a) Vertex (Alos/Palsar) DEM shaded relief image with solar azimuth (sun angle) of 45°, and a solar elevation of 30° (b) Map showing the distribution of lineaments extracted within the study area (c) Rose diagram of Measured Strike (d) Rose diagram of automatic lineament map, the overlapped yellow polygons are Abaya and Chamo Lake shape files.

Table 2. Parameter values selected as input for the automated feature extraction algorithm.

Description	Values	Description	Values
Filter Radius	10	Line Fitting Error	9
Edge Gradient	30	Angular Difference	30
Curve Length	30	Linking Distance	20

$$I_2 = \left(\left(G_{xx} \left(G_{yy} G_{zz} - G_{yz}^2 \right) + \left(G_{xy} \left(G_{yz} G_{xz} - G_{xy} G_{zz} \right) + \left(G_{xz} \left(G_{xy} G_{yz} - G_{xz} G_{yy} \right) \right) \right)^{\frac{1}{3}} \right. \quad (2)$$

Where I_1 and I_2 are Invariance of Tensors computed from all FTG components.

Tensor information is significant to identify target geology and also map the geological setting across any survey area. Invariance of Tensors I_1 and I_2 are computed using the Pedersen and Rasmussen (1990) technique shown (Figure 8a & b) respectively. According to Murphy and Brewster (2007) I_1 delineated the gross regional stratigraphy across survey areas identifying dominant density contrasts and I_2 identifies fault block geometries. Invariance of Tensor I_1 and I_2 (Figure 8a & b) is 500m upward continued to suppress the shallower and sharper anomaly resulted from higher frequency to accentuate the subsurface geological and tectonic settings of the area. I_1 delineated the gross regional stratigraphy across the area by identifying structurally controlled sub-basins with lower density contrasts in agreement with Bouguer anomaly (Figure 6) and Vertical Gravity Gradient G_{zz} (Figure 7f). The lower density contrasts of I_1 shows that Northern Abaya is structurally connected in N–S with Gelana basin to the south retaining NE-SW to the north and Southern Abaya and Chamo basins NE–SW direction. Invariance of Tensor I_2 (Figure 8b) identifies fault block geometries with high anomaly contrast on the sub basins dominantly NE–SW and N–S directions.

3.5. 3D Euler deconvolution

Euler deconvolution uses potential field derivatives or tensor gradients to image subsurface depth of a magnetic or gravity source (Hsu,

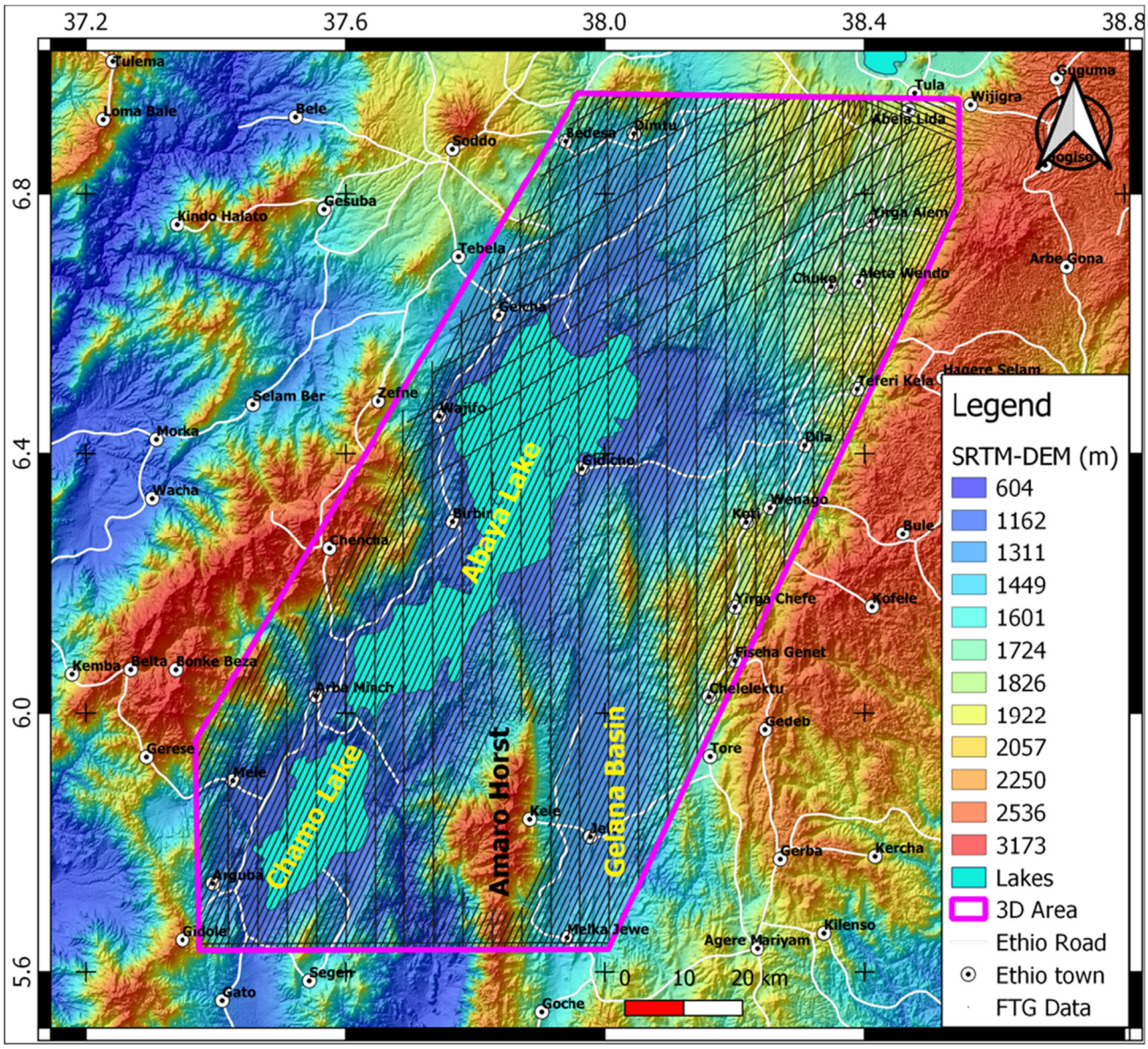

Figure 5. Location of the FTG data acquisition flight path on SRTM DEM of the study area.

2002). Reid et al. (1990) formulated a 3D form of Euler's equation can be defined using (Eq.3).

$$\frac{dg}{dx}(x-x_0)+\frac{dg}{dy}(y-y_0)+\frac{dg}{dz}(z-z_0)=-\eta g \tag{3}$$

Where $\frac{dg}{dx}$, $\frac{dg}{dy}$ and $\frac{dg}{dz}$ are independently measured derivatives of the field in the x, y and z directions , η is the structural index and (x_0, y_0 and z_0) are source locations.

3D Euler deconvolution technique was performing on the Bouguer gravity anomaly and Full tensor gravity components G_{xx}, G_{yy} and G_{zz} in an attempt to find depth to basement of lineaments. The structural index is chosen according to a prior knowledge of the source geometry of the area (Kebede and Mammo, 2021), contacts like faults have a structural index of 0 in gravity field so identifications of basement blocks faults are performed using index 0. Euler depth solution (Figure 9) show that the limits of the crystalline basement sources running between 2500 and 3500 m deep in rift basin area where Abaya Lake, Chamo Lake and Gelana basins resides.

3.6. Spectral analysis

The method is used to investigate the frequency content for estimation of the mean depth of the geological interfaces by the analysis of the Radial Power Spectrum of gravity field (Spector and Grant, 1970), thus the method describes the variation of the energy as a function of frequency to estimate subsurface depth given by (Eq.4).

$$h=\frac{1}{4\pi}\left(\frac{\log E_1-\log E_2}{K_1-K_2}\right) \tag{4}$$

Where E_1 and E_2 are power spectra of the gravity field, $\log E_1$ and $\log E_2$ are logarithms of the power spectra K_1 and K_2 are wave numbers and h is depth to interfaces (layer boundaries).

The log of Radial Power Spectrum of the vertical gravity gradient G_{zz} as a function of wave number or frequency (Blakely and Simpson, 1986), represented by (Figure 10) reflecting three linear depths: $h_1 = 3.58$km is the deep basement sources $h_2 = 2.45$km is the intermediate basement sources, $h_3 = 1.00$km associated with shallow volcano-sedimentary sources.

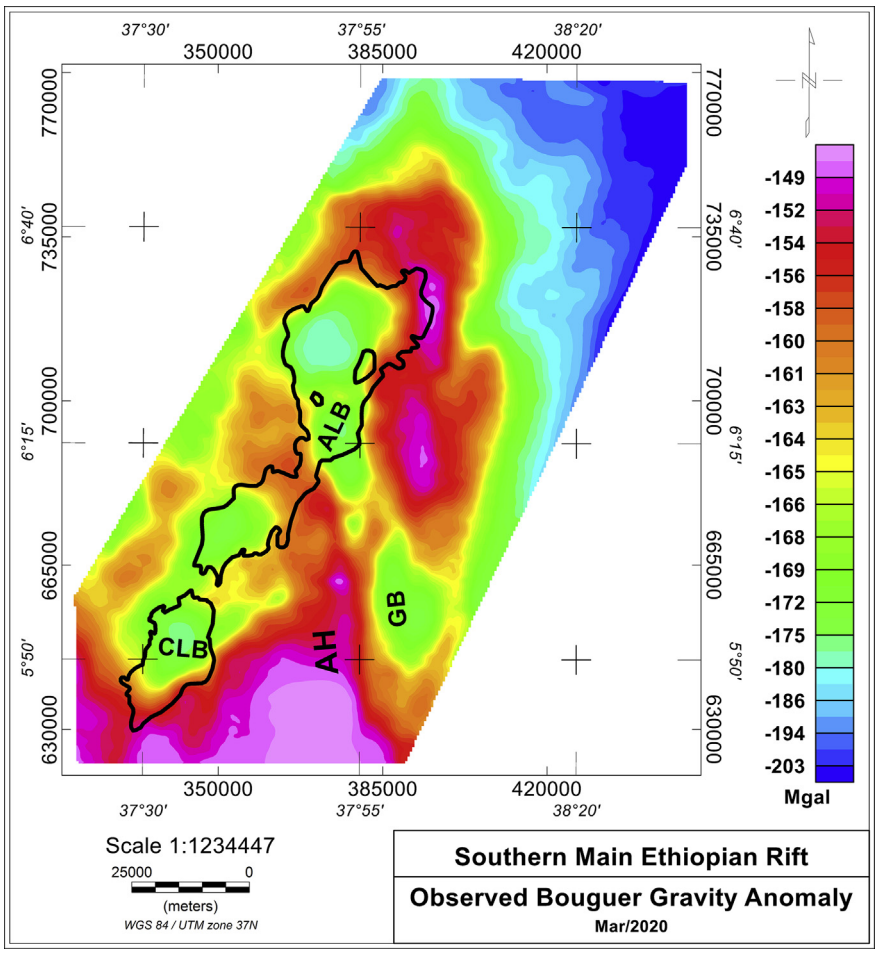

Figure 6. Complete Bouguer Gravity (g_z) anomaly map. ALB = Abaya Lake Basin, CLB = Chamo Basin, GB = Gelana Basin, and AH = Amaro Horst; the overlapped polygons are Abaya and Chamo Lake shape files.

3.7. Forward and inverse modeling

Parker (1973) introduced fast Fourier transform (FFT) into the forward calculation of the potential field interface Eq. (5).

$$F[\Delta g] = -2\pi G\rho e^{-|\overrightarrow{F}|z_o} \sum_{n=1}^{\infty} \frac{|\overrightarrow{k}|^{n-1}}{n!} F\left[h^n(\overrightarrow{r})\right] \tag{5}$$

Where $F[\,]$ denotes Fourier transformation, Δg is the gravity anomaly, G is the gravitational constant, ρ is the density contrast across the interface, $\overrightarrow{k}$ is the wavenumber (associated with the wavelength λ), z_o is the mean depth of the interface where the axis system has z vertically downward with $z_o > 0$, and $h(\overrightarrow{r})$ is the interface variation from the mean depth.

Oldenburg (1974) developed a frequency domain iterative inversion method of the density interface based on Parker (1973) algorism which gives faster computation using the fast Fourier transform Eq. (6).

$$F[h(\overrightarrow{r})] = -\frac{F[\Delta g]}{2\pi G\rho} e^{|\overrightarrow{k}|z_o} - \sum_{n=2}^{\infty} \frac{|\overrightarrow{k}|^{n-1}}{n!} F\left[h^n(\overrightarrow{r})\right] \tag{6}$$

Each symbol in Oldenburg formula Eq. (6) has the same meaning as in Parker formula Eq. (5). Eq. (6) may allow us to iterate the depth of the interface, but there is a non-convergent term $e^{|\overrightarrow{k}|z_o}$ to ensure convergence, he added a low-pass filter denoted by HCF (k) Eq. (7) to formula during the calculation.

$$HCF(k) = \begin{cases} 0, & if \quad \frac{k}{2\pi} > SH \\ \frac{1}{2}\left[1 + \cos\left(\frac{k - 2\pi WH}{2(SH - WH)}\right)\right], & if \quad WH \le \frac{k}{2\pi} \le SH \\ 1, & if \quad \frac{k}{2\pi} < WH \end{cases} \tag{7}$$

The HCF (k) filter passes all frequencies up to WH and does not pass any above the cutoff frequency SH is used to restrict the high frequency contents in the Fourier spectrum of the observed gravity anomaly. The smallest and greater cut-off frequency parameters are chosen from Spectral analysis (Figure 9) as $WH = 0.03$ km^{-1} and $SH = 0.06$ km^{-1}, respectively.

According to Bessoni et al. (2020) the RMSE (Root Mean Square Error) related to iterative optimization applied to obtain the basement depths using Oldenburg algorism, Eq. (8).

$$RMS = \sqrt{\sum_{i=1}^{n} \frac{\left(d^{obs} - d^{cal}\right)^2}{N}} \tag{8}$$

Where N is number of observation points , d_i^{obs} observed anomaly and d_i^{cal} calculated anomaly.

In this paper the structural inversion of the basement is performed using the Complete Bouguer gravity anomaly (g_z) (Figure 6) integrated with FTG components (G_{xx}, G_{yy}, G_{xy}, G_{xz}, G_{yz} and G_{zz}) (Figure 7 a-f). The GM-SYS 3D is an extension for Oasis Montaj software (Montaj, 2015) used for the purpose of detecting the depth to the top of the basement

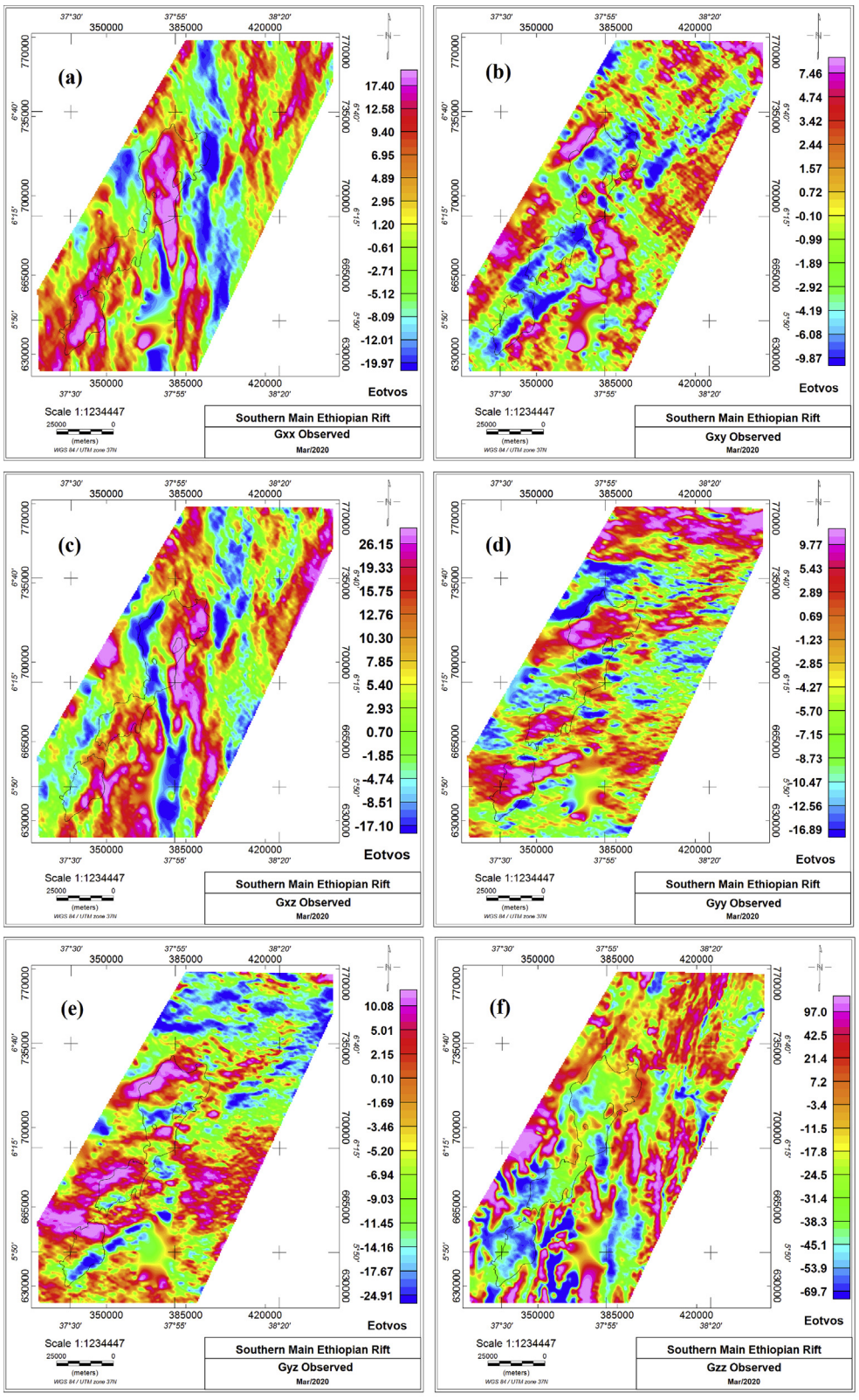

Figure 7. FTG components (a) G_{xx} (b) G_{xy} (c) G_{xz} (d) G_{yy} (e) G_{yz} and (f) G_{zz} anomaly maps: the overlapped polygons are Abaya and Chamo Lake shape files. Units of Gravity Gradients Eötvös, with 1 Eötvös equal to 0.1 mGal/km.

surface and 3-D modeling of subsurface structures, prevailing the studied area.

The Forward and inverse Modeling presented in this paper is summarized in (Figure 11) below.

A prior information is incorporated to address the nature of non-uniqueness in the inverse problem and the inversion process conducted as optimization problem (Ellis and Oldenburg, 1994; Jackson, 1979; Mammo, 2012, 2013; Mehanee and Essa, 2015). Since the subsurface

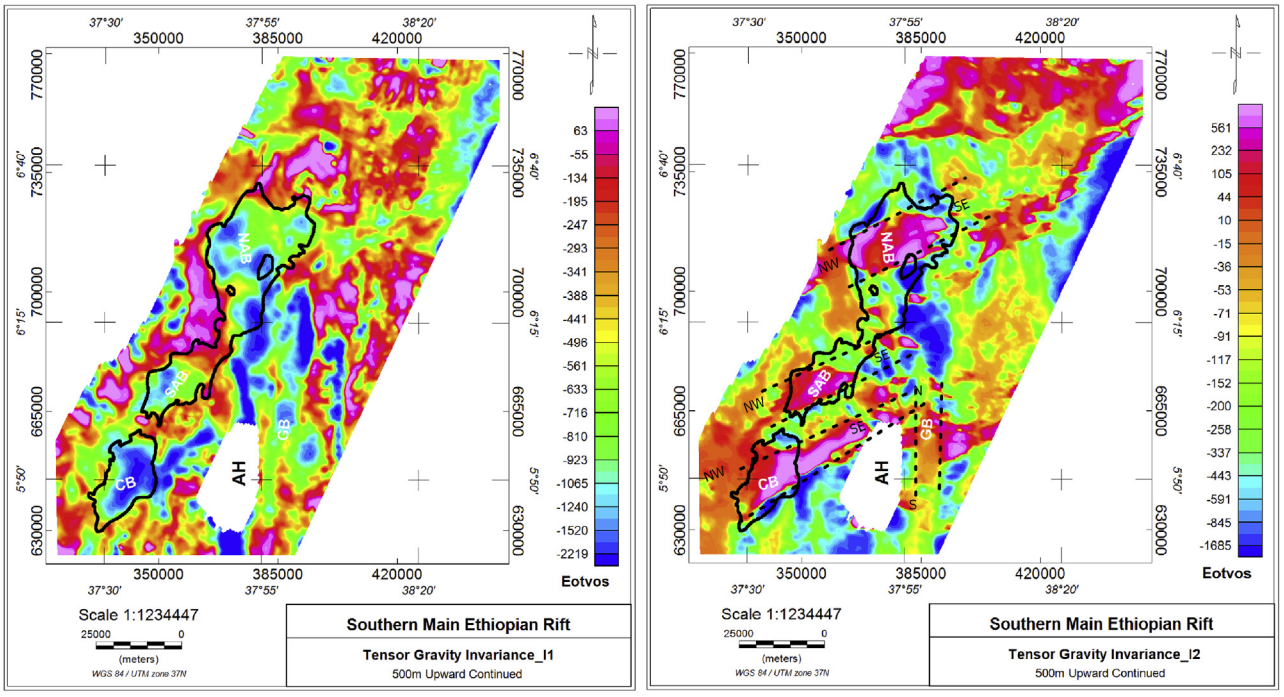

Figure 8. Invariant computation of the FTG data; (a) I_1 delineated the gross regional stratigraphy across the area using the density contrast (b) I_2 mapping subsurface fault blocks dominantly shows NE-SW directions.

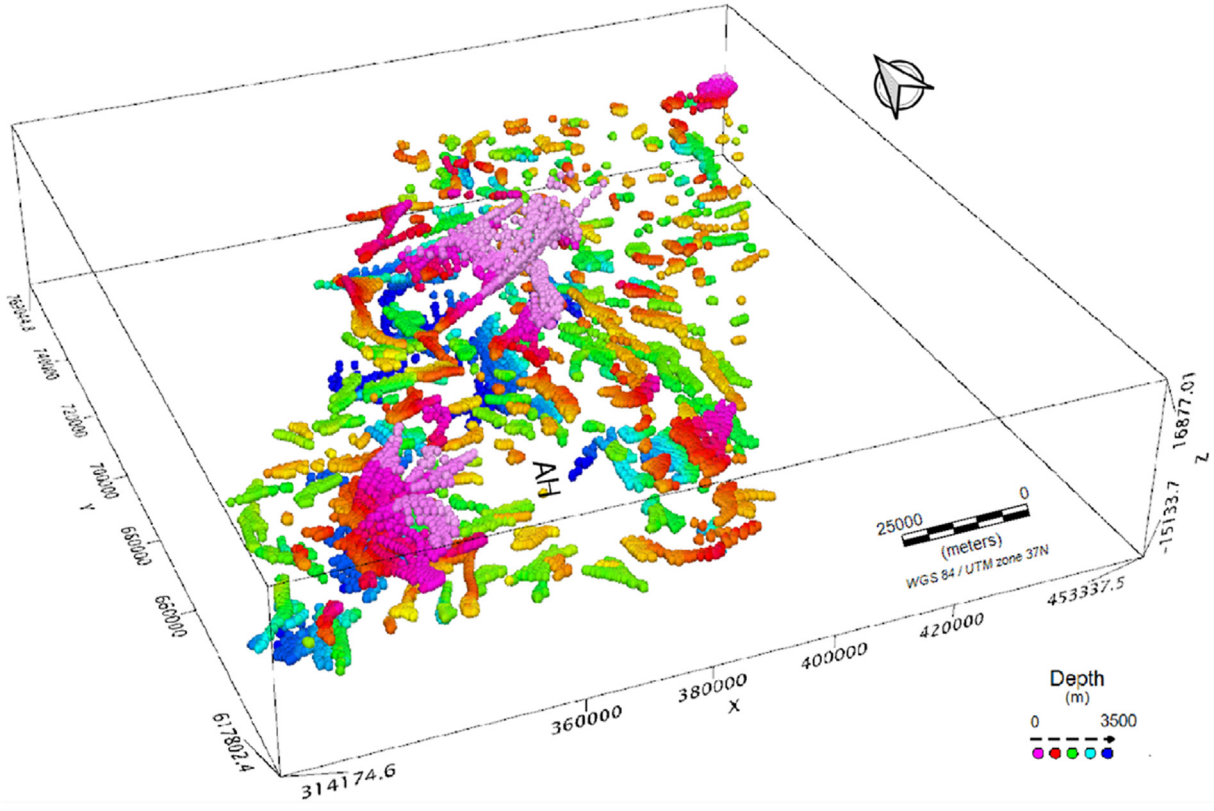

Figure 9. 3D Euler deconvolution solutions on Southern MER using a window size of 10 grid cells, a depth tolerance of 15% and a structure index 0: AH = Amaro Horst.

model derived from independent gravity modeling is not unique, plausible or reasonable model is defined using Auxiliary (a prior) information's by incorporating the results from geological field work, Euler Depth solutions (Figure 9) and Spectral depth estimations (Figure 10), Tilt Angle depth estimation (Kebede and Mammo, 2021), EAGLE controlled source wide-angle reflection/refraction P-Wave 2D seismic velocity models (Maguire et al., 2006) and nearby well data (Tullow Oil, 2014) to arrive at a more plausible geological model.

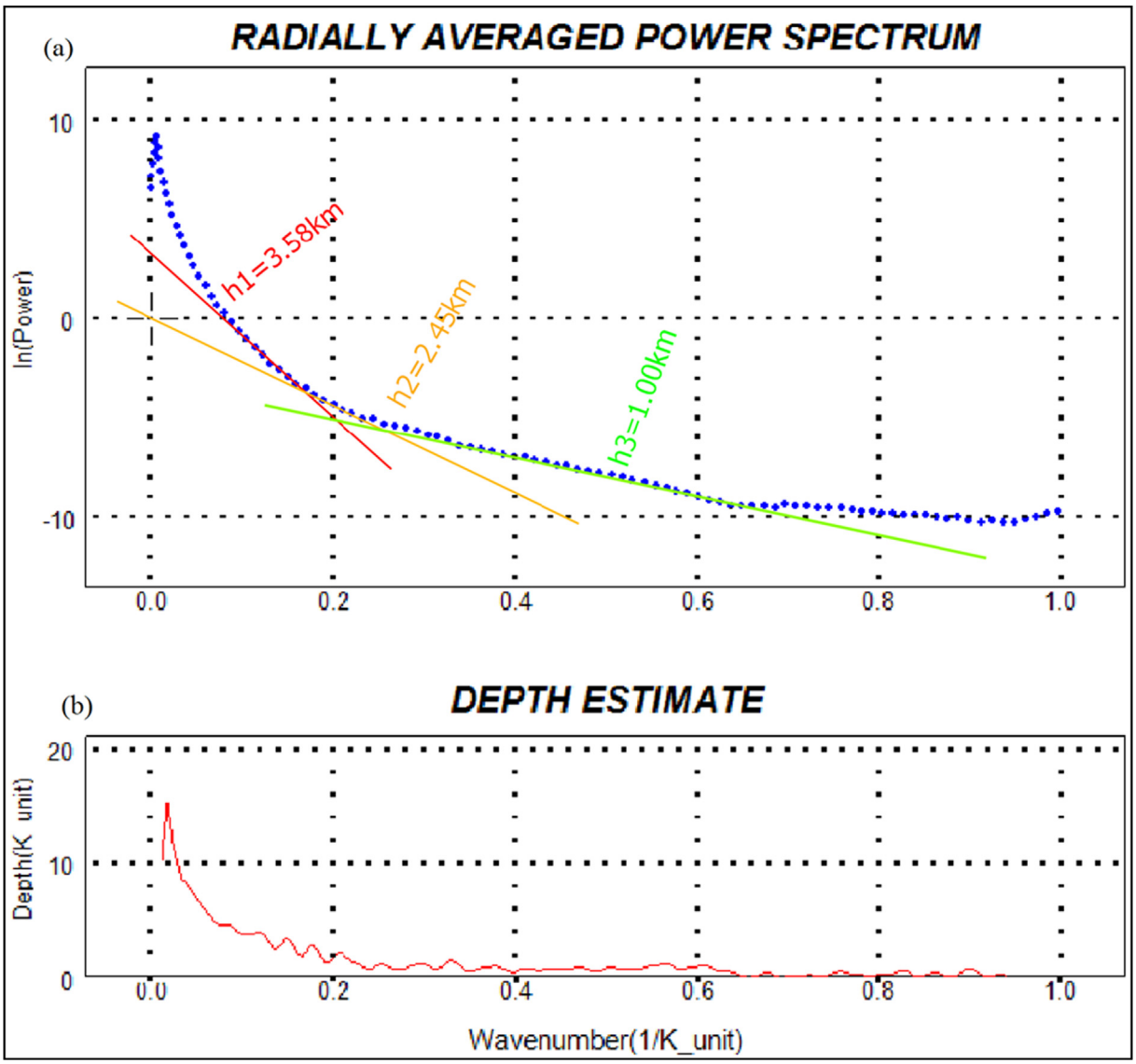

Figure 10. (a) Radial average of the energy spectrum versus the radial frequency (b) Estimated depth versus the radial frequency computed from vertical gravity gradient G_{zz} field.

The average (Mean) value of the basement interface density (ρ_2 ~2.6 gm/cm^3) determined from the field is equivalent to the density derived from P-Wave 2D seismic velocity models (Maguire et al., 2006) by considering P- wave velocity ($V_p = \sim 5km/s$) using a popular relation between density (ρ) and *P*-wave velocity (V_p) seems to be that of Gardner et al. (1974) the relation takes the following forms, depending on the units of V_p (in all cases the units of density are gm/cm^3):

For 1.50 km/s $\leq V_p <$ 6.0 km/s the density can be determined using Eq. (9)

$$\rho = 1.74V_p^{0.25} \tag{9}$$

The crystalline basement interface density (ρ_2 ~2.6 gm/cm^3) and volcano-sedimentary rocks density (ρ_1 ~2.4 gm/cm^3) are also determined from density log of Gardim-1 wells of Chew Bahir Basin (Tullow Oil, 2014). The average interface depth of the basement ($z_0 \sim$ 3400m) is derived from depth solutions of Euler deconvolution and Spectral depth estimations (Figure 9 and Figure 10) and depth estimations using Tilt Angle by Kebede and Mammo (2021).

An average density contrast of $\Delta\rho$ ~0.2 gm/cm^3 between the basement interface density (ρ_2 = 2.6 gm/cm^3) and the volcano-sedimentary rocks density (ρ_1 = 2.4 gm/cm^3) with mean interface depth of the basement $z_0 \sim$ 3400m are utilized to facilitate the structural inversion of the area of interest. The constrained inversion process is iterated by applying ten iterations until the fitting between the observed and calculated Bouguer gravity anomaly as well as Full Tensor Gravity (FTG) components (G_{xx}, G_{yy}, G_{xy}, G_{xz}, G_{yz} and G_{zz}) anomalies occurred with an average error lower than five percent (Figure 12b & Figure 13 a-f).

At the end of the iterative process, the program provides information to make three graphics: estimated 2D/3D topography of the Precambrian basement (Figure 14 & Figure 15b), predicted (calculated) gravity anomaly (Figure 12a & Figure 13 a-f) due to the estimated topography and Misfit or residual between the observed and predicted gravity anomalies (Figure 12 & Figure 13a-f). The RMS error obtained from iterative inversions of gravity and gravity gradients (FTG) are well below 0.1% (Figure 12c & Figure 13 a-f).

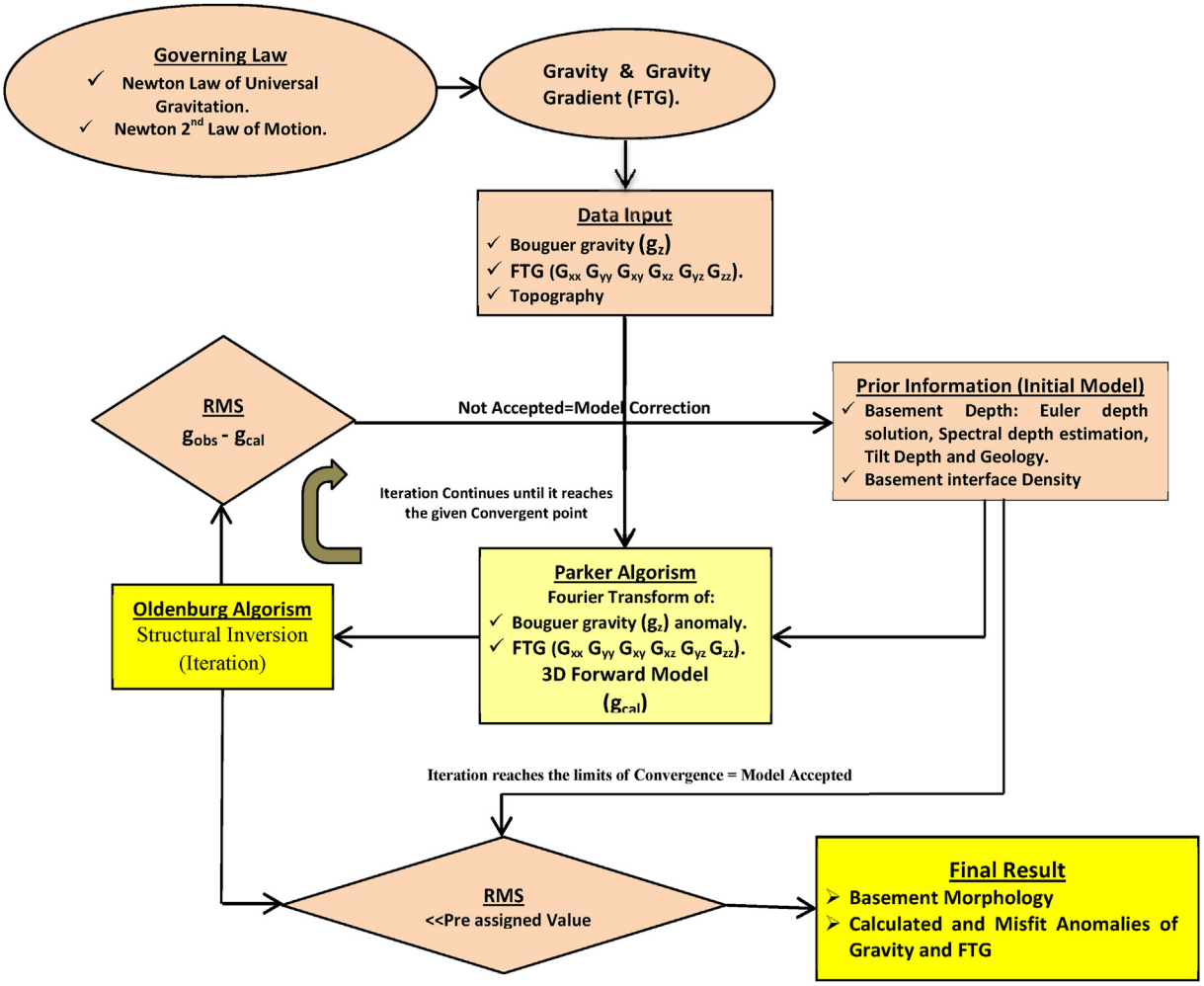

Figure 11. Summery of forward modeling and structural inversion.

4. Results and discussion

This paper presents a study of constraint 3D-density interface inversion of the crystalline basement of Southern MER using Bouguer gravity signal measured by Gravity Measurement Assembly (GMA) and independently measured components of Gravity Gradient Tensor fields (FTG) via FTGeX instrument in which investigations of the subsurface basement morphology integrated with the geology and tectonic setting is very crucial for the purpose of districts where there may be hydrocarbons. Geological field work conducted for determining the density of Precambrian basement rocks of the area (Table 1) shows that, the basement outcrops in Amaro Horst ridge and Chencha escarpment are dominated

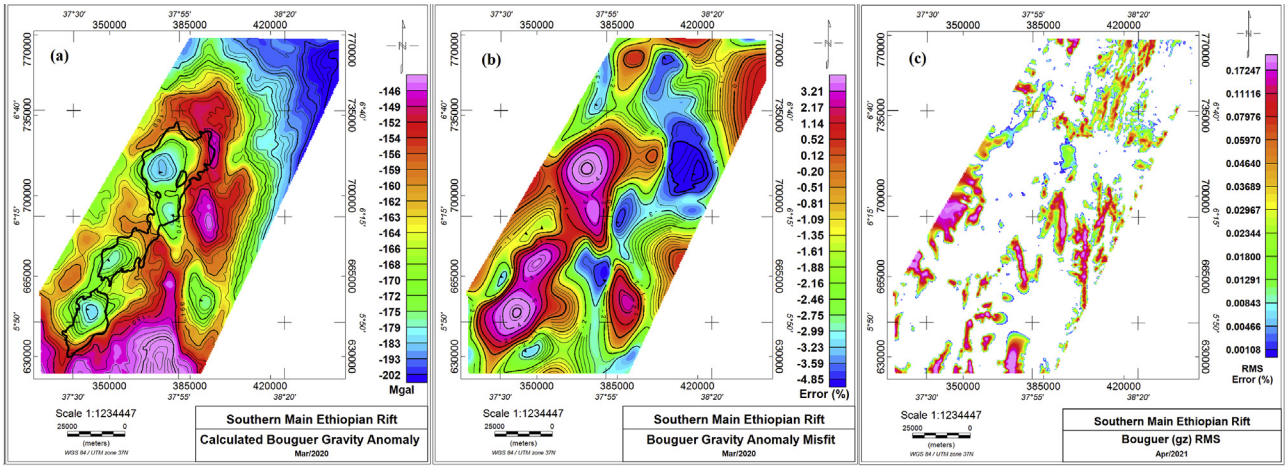

Figure 12. Bouguer gravity (g_z): (a) Calculated anomaly (Forward Model) (b) Misfit (c) RMS Error.

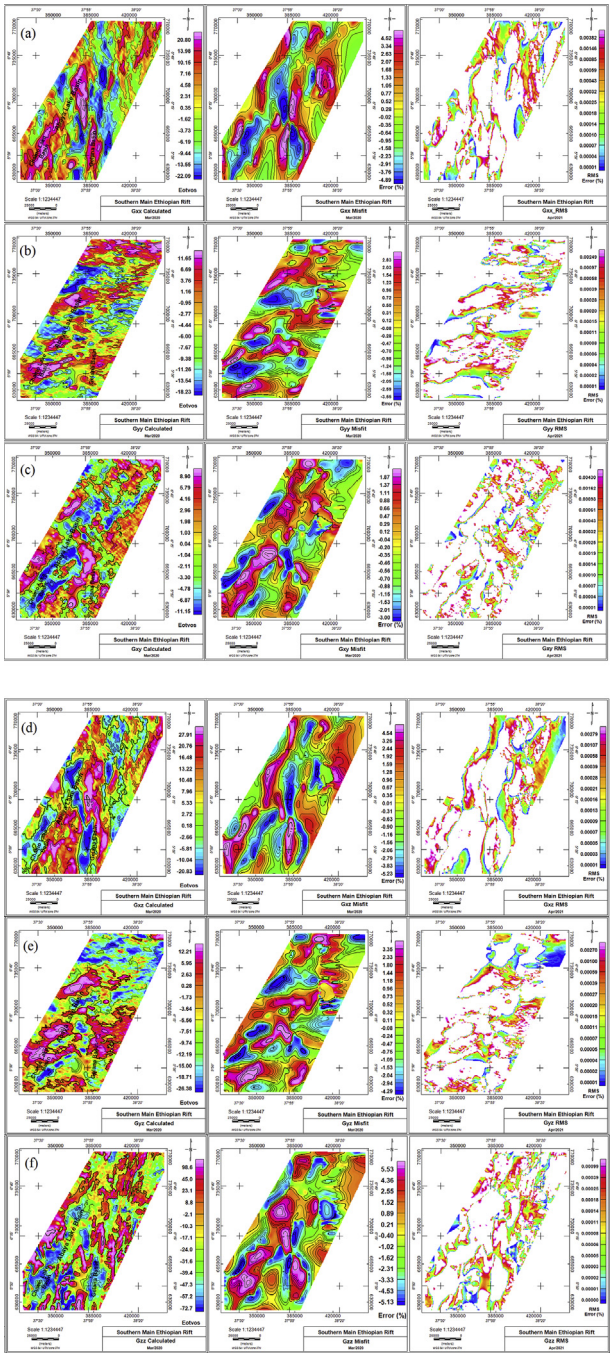

Figure 13. Full Tensor Gravity Components (FTG) (a) G_{xx} (b) G_{yy} (c) G_{xy} (d) G_{xz} (e) G_{yz} and (f) G_{zz} ; Calculated anomalies (Forward Models), Misfits and RMS Errors from left to right respectively.

by high grade gneisses (migmatite gneiss, Mafic Gneiss and Granitoid Gneiss) (Figure 3a-f) and Intrusive (Metagranite and Granodiorite). The Precambrian basement rock is overlain unconformably by Pre-Tertiary red Sandstone (Figure 3e) and the Lower Basalt: the oldest and most extensive of the volcanic unit in the area (Figure 2 & Figure 3f). More than 30 rock samples are collected along five traverses of total length 945km (Figure 2) and bulk density determination (Table 1) resulted in average density of (~2.6 gm/cm^3), this value is in agreement with density derived from density log of nearby Gardim-1 well on Chew Bahir Basin, Southern Ethiopian Rift (Tullow Oil, 2014) and density derived from P-Wave 2D seismic velocity models (Maguire et al., 2006). Field studies showed that in some localities of Amaro Horst crystalline basement is unconformably overlain by Pre-Tertiary or Mesozoic sedimentary rocks possibly extend into studied sub-basins with larger thickness than the elevated area where the unit is exposed. Multi-Layer 3D gravity forward modeling in northern parts of Ethiopia by Mammo (2010) and 2D/3D modeling of potential field data in Central MER by Kebede et al. (2021) shows that the existence of Mesozoic sediment overlaid on the Precambrian basement rock. Fieldwork conducted on southern part of Amaro Horst by WoldeGabriel et al. (1991) documented middle to late Miocene fossiliferous volcaniclastic lacustrine and fluvial sedimentary sequence interbedded with basaltic flows. The Mesozoic and middle to late Miocene fossiliferous volcaniclastic lacustrine sedimentary rocks are a proven oil-prone source unit in Jurassic – Cretaceous and Tertiary basins respectively (Macgregor et al., 2018; Purcell, 2007). Black shale and Lignite occur on the western rift margin, west of the Lake Abaya basin and initial organic geochemical analysis demonstrated that these are potential petroleum source rocks (Africa Oil Corp, 2014). Miocene source rocks with 5–7% TOC at early oil thermal maturity delineated in the Abaya Basin (Africa oil Corp, 2017). The results of measured structures (Table 1), DEM based extracted lineaments (Figure 4b) and Invariant Tensors computed using the Pedersen and Rasmussen (1990) technique (Figure 8b) showed that the study area has numerous heterogeneous fractures whose structural trends are oriented in NE–SW, NW–SE and N–S direction. Directional analysis performed on the measured structures and DEM extracted lineaments presented in a rose diagrams (Figure 4c) and (Figure 4d) generally showed that dominant trend tend to run in the NE–SW in Abaya and Chamo basins and N–S direction align with the axial portions of the Tertiary Ethiopian Rift which is also in agreement with fault block geometries identified by Invariance Tensor analysis (Figure 8b). These results have good correlation with the faults deduced from analysis and interpretation of Full Tensor Gravity (Kebede and Mammo, 2021) and known faults deduced from geological studies in the area (Asrat et al., 2001; Mengesha et al., 1996).

The observed Bouguer anomaly (Figure 6) shows variations from minimum of -200mGal to the maximum of -140mGal. Abaya Lake, Chamo Lake and Gelana basins are depicted by low amplitude gravity anomaly lower than -175mGal may be interpreted as a low density source rocks associated with pre-rift, post-rift and syn-rift sediment depositions. The Bouguer gravity anomaly in northern Abaya basin is approximately -180mGal, where the maximum basement depth of more than 3.7 km delineated. The regional Bouguer gravity anomaly of Omo basin in Southern Ethiopian Rift is below -140mGal (Purcell, 2007) in which 3D inversion of the residual gravity anomalies and automatic depth estimation techniques indicated that basement depth is estimated to be about 4 km on average (Mammo, 2012). In Lake Turkana Basin, North-western Kenya of Eastern branch of tertiary rift, the basement depth exceeds 5 km (Rop, 2012), where the regional Bouguer gravity anomaly is -100mGal on average (Purcell, 2007). On the Western branch of tertiary rift of Uganada, the basement depth of Albertine Basin in at circa 8 km (Macgregor, 2015), where the regional Bouguer gravity anomaly below is -220mGal (Nimmagadda et al., 2006). The Bouguer anomaly pattern agree with Invariance of Tensor anomaly (Figure 8a) delineated structurally controlled sub-basins with lower density contrasts may also shows the sediment infill of the sub-basins. Referring to the geological map of the area (Figure 2) lacustrine alluvium and eluvium are mostly prevalent at Abaya Lake, Chamo Lake and Gelana basins having relatively lower densities evidently contribute to low gravity as well as invariance of tensor anomalous zones over these areas. North-south trending high Bouguer anomaly deviated by 16.7 % from the mean value separating Gelana basin to the east from Chamo Lake basin to the west associated with the elevated metamorphic basement rock of Amaro Horst. This high values are also observed in the central parts of the area may be the extension of elevated Precambrian basement rock of Amaro Horst dive into the subsurface to the NW-SE direction parting Abaya Lake basin into two Northern and Southern structurally distinct sub-basins. The spectral energy spectrum (Figure 10) reflects the deep and intermediate basement sources of 3580 m and 2450 m respectively and the shallow volcano-sedimentary

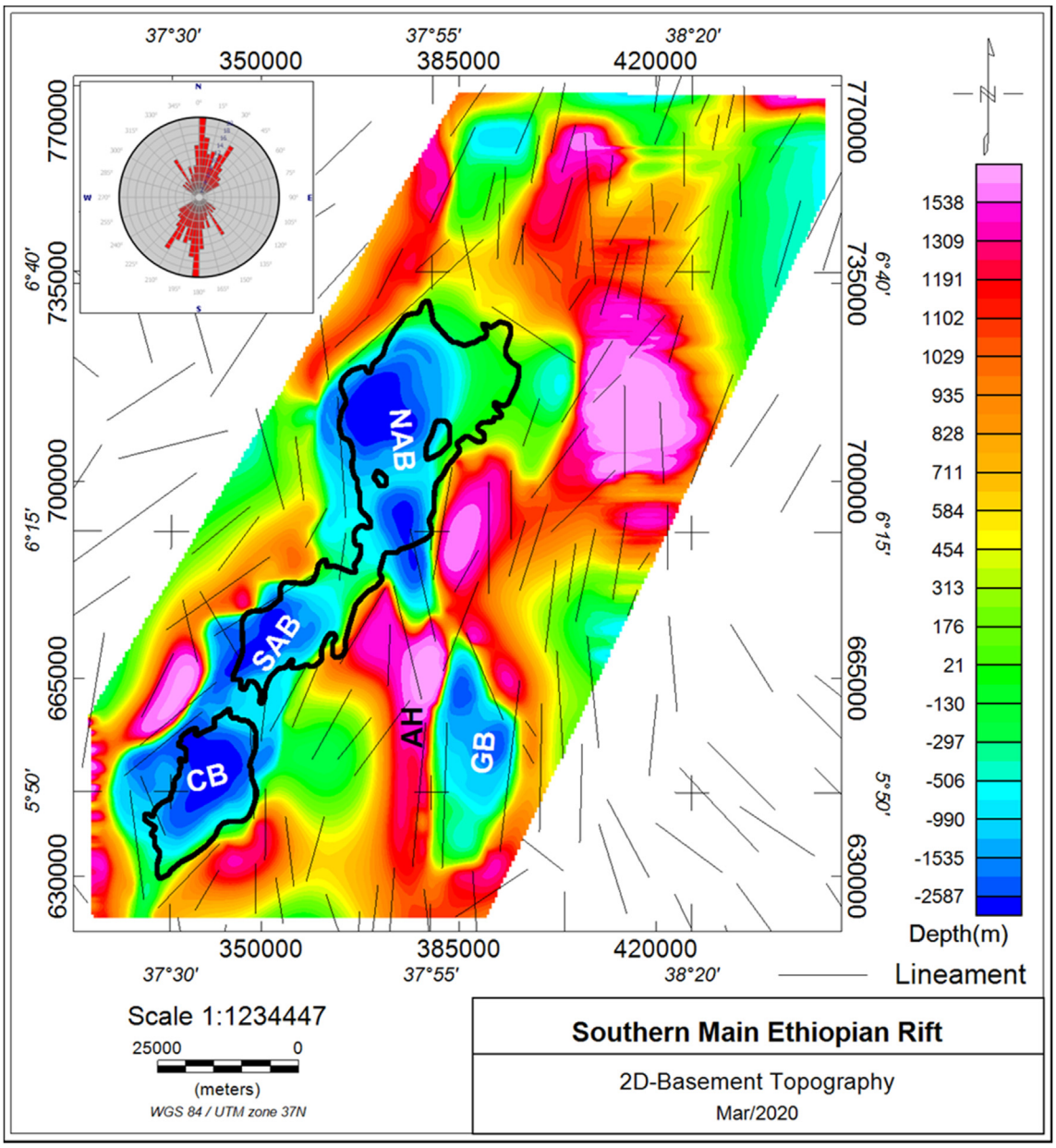

Figure 14. 2D-Basement relief (Inverse Model) map overlaid by extracted lineament: NBA = Northern Abaya Basin, SBA = Southern Abaya Basin, CB = Chamo Basin, GB = Gelana Basin and AH = Amaro Horst; the overlapped polygons are Abaya and Chamo Lake shape files.

sources having a depth less than 1000 m, this result agree with Euler deconvolution source depth solutions (Figure 9) that shows the limits of the crystalline basement sources running between 2500 m and 3500 m deep over the sub-basins. The basement inversion has been constrained using a priori information's, depth solutions of Euler deconvolution (Figure 8), Spectral depth estimations (Figure 10), depth estimations using Tilt Angle (Kebede and Mammo, 2021), P-wave 2D seismic velocity models (Maguire et al., 2006), nearby well data (Tullow Oil, 2014) and results from geological field work to minimize the non-uniqueness solutions of the potential field inversion. The constrained inversion process incorporate an average density contrast of (~0.2 g/cm^3) between the basement interface density (~2.6 gm/cm^3) and volcano-sedimentary rocks density (~2.4 gm/cm^3) with an average basement interface depth of (~3400 m), iterated ten times until a satisfactory agreement between observed and calculated Bouguer gravity (Figure 12) and FTG components are obtained. The topography of the study area (Figure 5 & Figure 15a) shows the surface elevations varies from a maximum value of more than 3200 m above sea level (a.s.l) in Amaro horst to a minimum value of 1123 m a.s.l in area where the Chamo Lake basin resides. The basement morphology (Figure 14 & Figure 15b) shows significant subsurface undulations in the area by clearly delineated four sub-basins residing in the area; Northern Abaya, Southern Abaya, Chamo and Gelana basins where the maximum depression exceeds a value 2500m below sea level (b.s.l) in Northern Abaya basin. The basement depth of Gelana basin is more than 2200 m b.s.l whereas in southern Abaya and Chamo basins the basement depth exceeds 2100 m b.s.l. This result agrees with Invariant Tensor (Figure 8a) that delineated structurally controlled sub-basins with lower density contrasts and Euler and Spectral source depths solutions (Figure 9 & Figure 10) that show the limits of the crystalline basement vary between 2500 and 3500m deep on the studied sub-basins.

Amaro Horst, a Precambrian basement rock, with surface elevation greater than 3200m a.s.l used as a control point in the inversion process has more than 2600m a.s.l high on the basement morphology (Figure 14 & Figure 15b), this may be due to the summit ridge and other high ground of Amaro Horst are capped by thicker Tertiary volcanic rocks

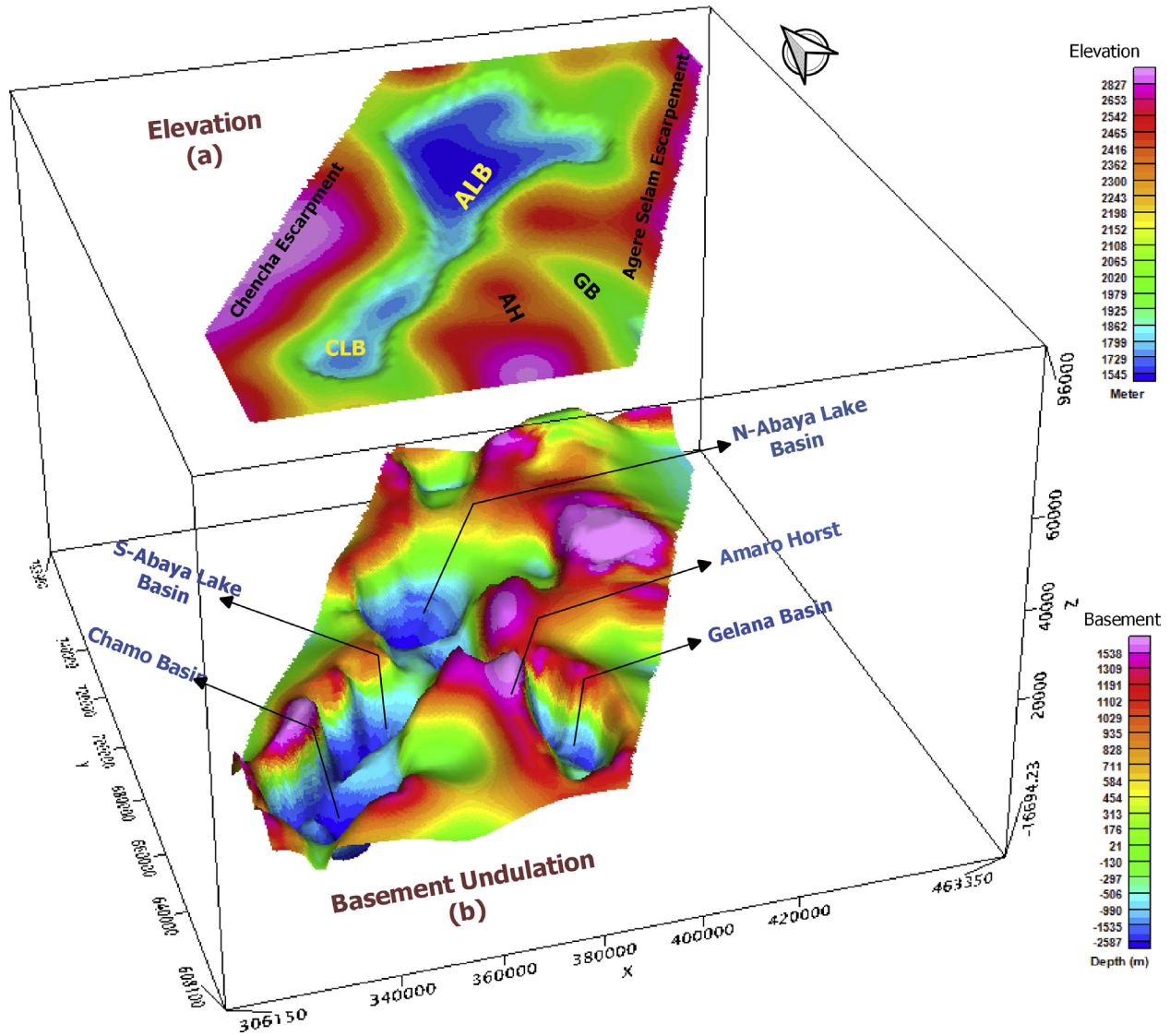

Figure 15. . (a) 3D-Elevation (b) 3D-Basement relief (Inverse Model) map; ALB = Abaya Lake Basin, CLB = Chamo Lake Basin, GB = Gelana Basin and AH = Amaro Horst.

(Levitte et al., 1974). Highly elevated areas of the rift margins such as Chencha and Agere Selam escarpment have also elevation exceeding 2400 m a.s.l.

Taking into account the surface topography (Figure 5 & Figure 15a) and the basement morphology (Figure 14 & Figure 15b) of the area, the total sediment thickness (Figure 16) in Northern Abaya and Gelana basins exceeds 3700m and 3500m respectively whereas in Southern Abaya and Chamo basins it is approximately 3300m. Amaro Horst, Chencha and Agere Selam escarpment are highly elevated areas having less sediment deposits ranging from 70 - 800m.

The basement morphology (Figure 14 & Figure 15b) depicted that the geologically inferred Abaya Lake basin is divided into Northern and Southern Abaya basins with northern part structurally connected with Gelana basin and the southern part connected to Chamo basin. This result agrees with the computed Invariant Tensors anomaly (Figure 8a) that identifies the structurally controlled sub-basins with lower density contrast. The most significant feature of the morphology of the basement is in defining the subsurface geometry of the sub-basins of the area, that is, the pure N–S elongated basement depression in Gelana basin and NE–SW trending basement depression observed in Southern Abaya and Chamo Lake basins in agreement with structural analysis in this study as well as previous works that show prominent N–S Precambrian faulting of the area (Asrat et al., 2001). The northern Abaya basin has complex structural configurations with NNW–SSE elongated structure in southern parts tend to connect with Gelana basin and fitting with the regional structural trends in northern part, bend from the older NW–SE Mesozoic rift orientation in the south to the younger Tertiary rift NE-SW orientation to the north (Figure 14 & Figure 15b). The complex structural patterns of the area may be the results of NNE–SSW Tertiary rift system the youngest and most active faults perpendicularly cross-cut by the pre-existing NW–SE Mesozoic Ogaden rift faults (Korme et al., 2004). The N–S oriented topographic high separating Gelana basin to the east from Chamo Lake basin to the west is anticlines in Amaro Horst, the Precambrian basement trough plunges into the Gelana basins. The basement morphology (Figure 14 & Figure 15b) revealed the nature of the subsurface geometry related to Southern MER in which the result agrees with the structural analysis as well as previous regional studies on directions of prominent geological structures. According to Bosworth (1985) and Rosendahl (1987) continental rift zones comprise a series of discrete and kinematically linked fault-bounded sedimentary basins created due to repeated episodes of faulting over millions of years, thus boundaries between Horst (uplifts) and Grabens (Depressions) in the basement undulation of the area may have been generated by the evolution of faulting due to the tectonic activities of various geological times.

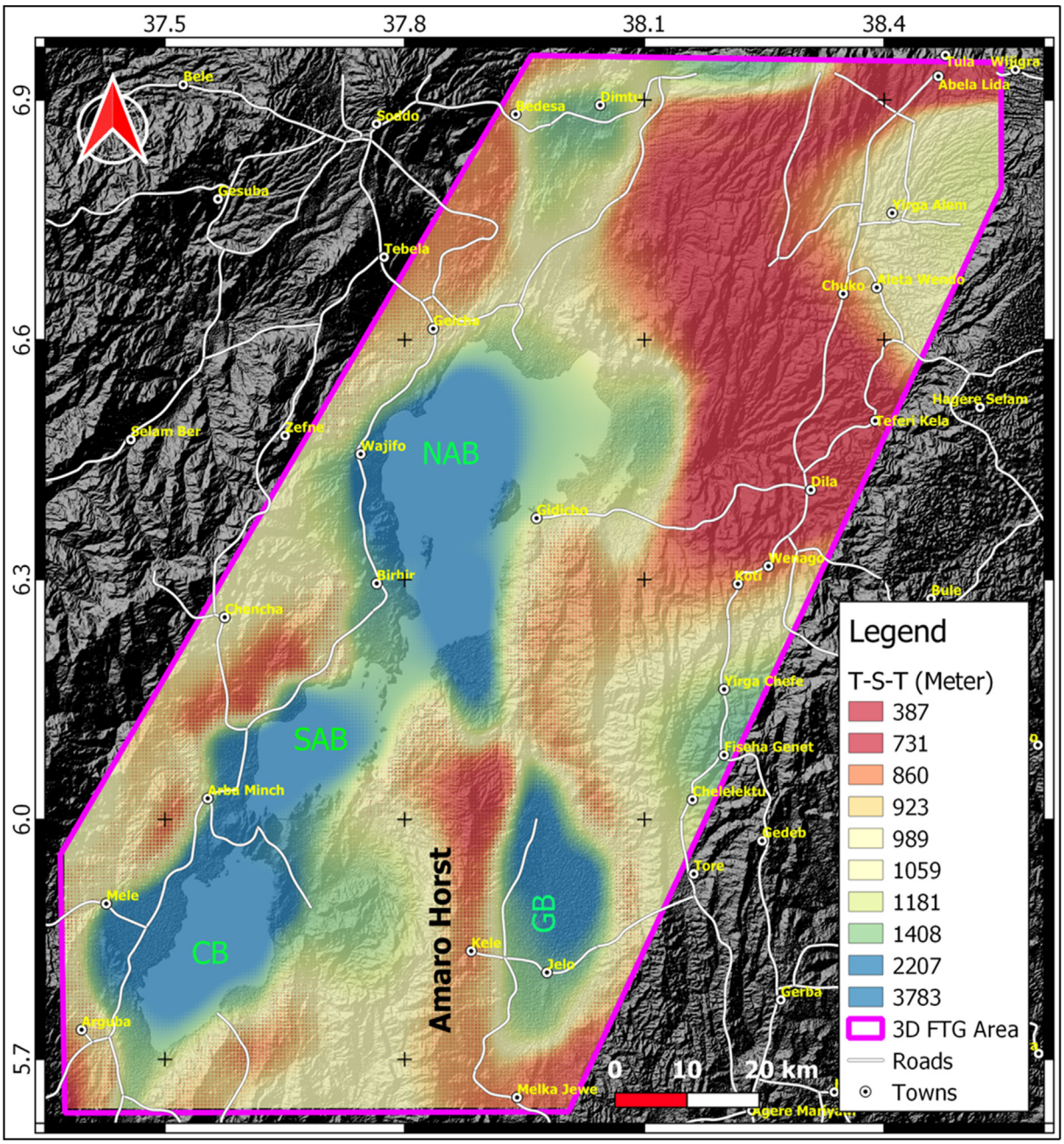

Figure 16. Total sediment thicknesses (T.S.T) of Southern MER basin and adjacent plateau: NBA = Northern Abaya Basin, SBA = Southern Abaya Basin, CB = Chamo Basin, GB = Gelana Basin.

Generally the basement morphology depicted the structurally controlled sub-basins having sufficient sediment thickness for potential hydrocarbon generation and accumulation and in continental rift basins fault closures against the basement, horst and grabens are the dominant structural paly provide a smooth hydrocarbon trapping mechanism, while the primary migration may take place along the fractured planes (faults) or pores within rock units.

5. Conclusion

This study has made use of a high resolution vertical gravity integrated with Full Tensor Gravity (FTG) datasets to recover the subsurface structural as well as geological units of Southern MER basin in order to determine the petroleum potentials of the area. Geological field work conduced over the area shows that the Precambrian basement outcrops are dominated by High grade gneisses and Intrusive with an average density value 6 gm/cm^3. Field studies on Amaro Horst showed that the basement is unconformably overlain by Mesozoic sedimentary rock, a proven oil-prone source as well as reservoirs unit in Jurassic – Cretaceous; possibly extend into studied sub-basins (grabens) with larger thickness than the elevated area where the unit is observed. In addition, the extracted lineaments from digital elevation model show that NE–SW, NW–SE and N–S directions with dominant direction align with regional structural trends NE–SW. Analysis of the Bouguer gravity and Invariance Tensor anomaly identified a structurally controlled sub-basins characterized by low (below -175mGal) anomalous zones may show that the predominant sediment infill of the areas. The Precambrian basement morphology of the area is delineated using constrained Tensor Gravity Inversion by applying the Parker–Oldenburg algorisms. The basement structural low depicts the sub-basins; Northern Abaya, Southern Abaya,

Chamo and Gelana basins, where the deepest depression exceeds 2500 m b.s.l. in Northern Abaya basin. This result agrees with Spectral and Euler source depths solutions that show the limits of the crystalline basement vary between 2500m and 3500m deep on the studied sub-basins. The maximum total sediment thickness is observed in northern Abaya basin which is more than 3700m whereas on the basement structural high like Amaro Horst, Chencha and Agere Selam escarpments the average sediment thickness is 500m. The basement morphology revealed the nature of the subsurface geometry related to Southern MER by clearly delineated the N–S orientations of Gelana basin with northern Abaya, southern Abaya and Chamo basins align with NE–SW Tertiary Rifting. This result agrees with the structural analysis as well as previous regional studies on directions of prominent geological structures. Finally the basement morphology depicted the structurally controlled sub-basins having sufficient sediment thickness for potential hydrocarbon generation and accumulation, can also possibly provide structural trapping mechanisms for the generated hydrocarbon.

Declarations

Author contribution statement

Bisrat Kebede: Conceived and designed the experiments; Performed the experiments; Analyzed and interpreted the data; Contributed reagents, materials, analysis tools or data; Wrote the paper.

Tilahun Mammo: Analyzed and interpreted the data; Contributed reagents, materials, analysis tools or data; Wrote the paper.

Abebe Misgie: Contributed reagents, materials, analysis tools or data; Wrote the paper.

Funding statement

This research did not receive any specific grant from funding agencies in the public, commercial, or not-for-profit sectors.

Data availability statement

The data that has been used is confidential.

Declaration of interests statement

The authors declare no conflict of interest.

Additional information

Supplementary content related to this article has been published online at https://doi.org/10.1016/j.heliyon.2022.e09525.

Acknowledgements

We would like to thank Ministry of Mines and Petroleum for providing the Full Tensor Gravity (FTG) data as well as allow us to use various reports and supporting the geological field work conducted in the study area. We also thank Geological Survey of Ethiopia for providing Laboratory assistance for determinations of the density of various rock samples. Getahun Mesesret (Geologist) and Kasshun Tsehay (Driver) thanked for their help in assisting the field work.

References

Abbate, E., Sagri, M., 1980. Volcanites of Ethiopian and Somali Plateaus and major tectonic lines. Atti Convegni Lincei 47, 219–227.
Abebe, T., Mazzarini, F., Innocenti, F., Manetti, P., 1998. The Yerer-Tullu Wellel volcanotectonic lineament: a transtensional structure in central Ethiopia and the associated magmatic activity. J. Afr. Earth Sci. 26 (1), 135–150.
Africa oil Corp, 2017. Corporate Presentation: Moving Forward to Development.
Africa Oil Corp, 2013. ARKeX Air FTG® Data Acquisition Report on Rift Valley Basin Block, Ethiopia. Unpublished Report, Ministry of Mines and Petroleum, pp. 1–37. Addis Ababa, Ethiopia. ARX-13501.
Africa Oil Corp, 2014. Rift Valley Block, Ethiopia Field Geology Update. Ministry of Mines and Petroleum, Addis Ababa, Ethiopia, pp. pp_34–35. Unpublished report.
AOC and MoM, 2011. Ethiopian Rift Valley Geological Reconnaissance, Unpublished Report, Africa Oil Corporation and Ethiopian Ministry of Mines Joint Study, pp. 39–43. Addis Ababa, Ethiopia.
Asrat, A., Barbey, P., Gleizes, G., 2001. The Precambrian geology of Ethiopia: a review. Afr. Geosci. Rev. 8 (3/4), 271–288.
Batson, R.M., Edwards, K., Eliason, E.M., 1975. Computer-generated shaded-relief images. J. Res. US Geol. Surv. 3 (4), 401–408.
Bellahsen, N., Faccenna, C., Funiciello, F., Daniel, J.M., Jolivet, L., 2003. Why did Arabia separate from Africa? Insights from 3-D laboratory experiments. Earth Planet Sci. Lett. 216 (3), 365–381.
Bessoni, T.P., Bassrei, A., Oliveira, L.G. S. de., 2020. Inversion of satellite gravimetric data from recôncavo-tucano-jatobá basin system. Braz. J. Genet. 50 (3).
Blakely, R.J., 1995. Potential Theory in Gravity and Magnetic Applications. Cambridge University, Cambridge.
Blakely, Richard J., Simpson, R.W., 1986. Approximating edges of source bodies from magnetic or gravity anomalies. Geophysics 51 (7), 1494–1498.
Bosworth, W., 1985. Geometry of propagating continental rifts. Nature 316 (6029), 625–627.
Braitenberg, C., Mariani, P., Ebbing, J., Sprlak, M., 2011. The enigmatic Chad lineament revisited with global gravity and gravity-gradient fields. Geol. Society London Spec. Pub. 357 (1), 329–341.
Cordell, L., Henderson, R.G., 1968. Iterative three-dimensional solution of gravity anomaly data using a digital computer. Geophysics 33 (4), 596–601.
Corwin, R.F., Ward, S.H., 1990. The self-potential method for environmental and engineering applications. Geotech. Environ. Geophys. 1, 127–145.
Davidson, A., 1983. The Omo river project, reconnaissance geology and geochemistry of parts of Ilubabor, Kefa, Gemu Gofa and Sidamo, Ethiopia. Ethiop. Inst. Geol. Surv. Bull. 2, 1–89.
Dickinson, J.L., Murphy, C.A., Robinson, J.W., 2010. Analysing full tensor gravity data with intuitive imaging techniques. In: 72nd EAGE Conference and Exhibition-Workshops and Fieldtrips (p. cp-161). European Association of Geoscientists & Engineers.
Ebinger, C.J., Yemane, T., Harding, D.J., Tesfaye, S., Kelley, S., Rex, D.C., 2000. Rift deflection, migration, and propagation: linkage of the Ethiopian and Eastern rifts, Africa. Geol. Soc. Am. Bull. 112 (2), 163–176.
Ebinger, C.J., Yemane, T., WoldeGabriel, G., Aronson, J.L., Walter, R.C., 1993. Late Eocene–Recent volcanism and faulting in the southern main Ethiopian rift. J. Geol. Soc. 150 (1), 99–108.
Ekinci, Y.L., Balkaya, Ç., Göktürkler, G., Özyalın, Ş., 2021. Gravity data inversion for the basement relief delineation through global optimization: a case study from the Aegean Graben System, western Anatolia, Turkey. Geophys. J. Int. 224 (2), 923–944.
Ellis, R.G., Oldenburg, D.W., 1994. Applied geophysical inversion. Geophys. J. Int. 116 (1), 5–11.
Feng, J., Zhang, S., Meng, X., 2015. Constraint 3D density interface inversion from gravity anomalies. Arabian J. Geosci. 9 (1), 56.
Ganas, A., Pavlides, S., Karastathis, V., 2005. DEM-based morphometry of range-front escarpments in Attica, central Greece, and its relation to fault slip rates. Geomorphology 65 (3–4), 301–319.
Gardner, G.H.F., Gardner, L.W., Gregory, A.R., 1974. Formation velocity and density—the diagnostic basics for stratigraphic traps. Geophysics 39 (6), 770–780.
Geomatica, P.C.I., 2013. PCI Geomatica User's Guide Version 2013.
Ghebreab, W., 1998. Tectonics of the red sea region reassessed. Earth Sci. Rev. 45 (1–2), 1–44.
Gubbins, D., 2004. Time Series Analysis and Inverse Theory for Geophysicists. Cambridge University Press.
Hinze, W.J., 1990. The role of gravity and magnetic methods in engineering and environmental studies. In: Geotechnical an Environmental Geophysics: Volume I: Review and Tutorial. Society of Exploration Geophysicists, pp. 75–126.
Hsu, S., 2002. Imaging magnetic sources using Euler's equation. Geophys. Prospect. 50 (1), 15–25.
Ingersoll, R.V., 1988. Tectonics of sedimentary basins. Geol. Soc. Am. Bull. 100 (11), 1704–1719.
Jackson, D.D., 1979. The use of a priori data to resolve non-uniqueness in linear inversion. Geophys. J. Int. 57 (1), 137–157.
Kebede, B., Mammo, T., 2021. Processing and interpretation of full tensor gravity anomalies of Southern Main Ethiopian Rift. Heliyon 7 (4), e06872.
Kebede, H., Alemu, A., Nedaw, D., Fisseha, S., 2021. Depth estimates of anomalous subsurface sources using 2D/3D modeling of potential field data: implications for groundwater dynamics in the Ziway-Shala Lakes Basin, Central Main Ethiopian Rift. Heliyon 7 (4), e06843.
Klein, G. deV., 1990. Maturation-based geodynamic/geochemical classification of sedimentary basins. Sediment. Geol. 69 (1–2), 1–6.
Klemme, H.D., 1980. Petroleum basins–classifications and characteristics. J. Petrol. Geol. 3 (2), 187–207.
Korme, T., Acocella, V., Abebe, B., 2004. The role of pre-existing structures in the origin, propagation and architecture of faults in the Main Ethiopian Rift. Gondwana Res. 7 (2), 467–479.
Levitte, D., Columba, J., Mohr, P., 1974. Reconnaissance geology of the Amaro horst, southern Ethiopian rift. Geol. Soc. Am. Bull. 85 (3), 417–422.
Macgregor, D., 2015. History of the development of the East African Rift System: a series of interpreted maps through time. J. Afr. Earth Sci. 101, 232–252.

Macgregor, D., Argent, J., Sansom, P., 2018. Introduction to the Thematic Set: Tectonics and Petroleum Systems of East Africa. Geological Society of London.
Maguire, P.K.H., Keller, G.R., Klemperer, S.L., Mackenzie, G.D., Keranen, K., Harder, S., Khan, M.A., 2006. Crustal structure of the northern Main Ethiopian Rift from the EAGLE controlled-source survey; a snapshot of incipient lithospheric break-up. Geol. Society London Spec. Pub. 259 (1), 269–292.
Mammo, T., 2010. Delineation of sub-basalt sedimentary basins in hydrocarbon exploration in North Ethiopia. Mar. Petrol. Geol. 27 (4), 895–908.
Mammo, T., 2012. Analysis of gravity field to reconstruct the structure of Omo basin in SW Ethiopia and implications for hydrocarbon potential. Mar. Petrol. Geol. 29 (1), 104–114.
Mammo, T., 2013. Crustal structure of the flood basalt province of Ethiopia from constrained 3-D gravity inversion. Pure Appl. Geophys. 170 (12), 2185–2206.
Mehanee, S.A., Essa, K.S., 2015. 2.5 D regularized inversion for the interpretation of residual gravity data by a dipping thin sheet: numerical examples and case studies with an insight on sensitivity and non-uniqueness. Earth Planets Space 67 (1), 1–26.
Mengesha, T., Tadiwos, C., Workneh, H., 1996. The Geological Map of Ethiopia, 1: 2,000,000 Scale. *Ethiopia*. EIGS Addis Ababa.
Menke, W., 2018. Geophysical Data Analysis: Discrete Inverse Theory. Academic Press.
Miall, A.D., 1995. Collision-related foreland basin. Tectonic. Sediment. Basins 393–424.
Mohr, P.A., 1962. The Geology of Ethiopia. Univ. Coll. Press, Addis Ababa, p. 268.
Mohr, P.A., Gouin, P., 1967. Gravity traverses in Ethiopia (third interim report). Bull. Geophys. Obs. Addis Ababa 10, 15–52.
Montaj, G.O., 2015. Data Processing and Analysis Systems for Earth Science Applications (Ver. 8.3. 3). Geosoft Inc, Toronto, Canada. *Accessed*.
Morley, C.K., Wescott, W.A., Stone, D.M., Harper, R.M., Wigger, S.T., Karanja, F.M., 1992. Tectonic evolution of the northern Kenyan Rift. J. Geol. Soc. 149 (3), 333–348.
Murphy, C.A., 2004. The Air-FTG airborne gravity gradiometer system. Airborne Gravity 7–14.
Murphy, C.A., Brewster, J., 2007. Target delineation using full tensor gravity gradiometry data. ASEG Extend. Abst. 2007 (1), 1–3.
Nimmagadda, S.L., Kashambuzi, R., Rubondo, E., Kasande, R., 2006. Application of integrated geophysical strategies in the albertine graben and its petroleum potentiality. In: AAPG International Conference and Exhibition. Perth, Australia.
Oldenburg, D.W., 1974. The inversion and interpretation of gravity anomalies. Geophysics 39 (4), 526–536.
Parker, R.L., 1973. The rapid calculation of potential anomalies. Geophys. J. Int. 31 (4), 447–455.
Paterson, N.R., Reeves, C.V., 1985. Applications of gravity and magnetic surveys: the state-of-the-art in 1985. Geophysics 50 (12), 2558–2594.
Pedersen, L.B., Rasmussen, T.M., 1990. The gradient tensor of potential field anomalies: some implications on data collection and data processing of maps. Geophysics 55 (12), 1558–1566.
Purcell, P.G., 1981. Phanerozoic Sedimentary History and Petroleum Potential. Plate Tectonics and Metallogenesis: Some Guidelines to Ethiopian Mineral Deposits, 2. Ethiopian Institute of Geological Surveys Bulletin, pp. 97–114.
Purcell, P.G., 2007. The Hydrocarbon Potential of the Ethiopian Tertiary Rift Basins, International Scientific Conference 50th Anniversary of the Founding of the Geophysical Observatory of Addis Ababa University. P&R Geological Consultants Pty Ltd, Perth, Western Australi.
Rao, D.B., Babu, N.R., 1991. A rapid method for three-dimensional modeling of magnetic anomalies. Geophysics 56 (11), 1729–1737.
Reddy, G.P.O., Mouli, K.C., Srivastav, S.K., Srinivas, C.V., Maji, A.K., 2000. Evaluation of ground water potential zones using remote sensing data-A case study of Gaimukh watershed, Bhandara District, Maharashtra. J. Ind. Soc. Remote Sens. 28 (1), 19–32.
Reid, A.B., Allsop, J.M., Granser, H., Millett, A. J. t, Somerton, I.W., 1990. Magnetic interpretation in three dimensions using Euler deconvolution. Geophysics 55 (1), 80–91.
Rop, B.K., 2012. Subsurface depositional systems in Lake Turkana basin, North-western Kenya: based on gravity and seismic data investigations. In: Proceedingd of the 4th African Rift Geothermal Conference, pp. 21–23.
Rosendahl, B.R., 1987. Architecture of continental rifts with special reference to East Africa. Annu. Rev. Earth Planet Sci. 15 (1), 445–503.
Sabins Jr., F.F., 1987. Remote Sensing-Pprinciples and Interpretation. WH Freeman and company.
Sankar, K., 2002. Evaluation of groundwater potential zones using remote sensing data in Upper Vaigai river basin, Tamil Nadu, India. J. Ind. Soc. Remote Sens. 30 (3), 119–129.
Spector, A., Grant, F.S., 1970. Statistical models for interpreting aeromagnetic data. Geophysics 35 (2), 293–302.
Tucker, M.E., 2009. Sedimentary Petrology: an Introduction to the Origin of Sedimentary Rocks. John Wiley & Sons.
Tullow Oil, 2014. Gardim-1 Geological Well Completion Report South Omo Block Chew Bahir Basin,Unpublished Report. Ministry of Mines and Petroleum, Addis Ababa, Ethiopia, p. 47.
Vittala, S.S., Govindaiah, S., Honne Gowda, H., 2006. Digital Elevation Model (DEM) for identification of groundwater prospective zones. J. Ind. Soc. Remote Sens. 34 (3), 319–324.
WoldeGabriel, G., Aronson, J.L., 1986. Volcanotectonic history of the main Ethiopian rift. In: Abstracts with Programs, International Volcanological Congress, p. 325. Auckland, New Zealand.
WoldeGabriel, G., Yemane, T., Suwa, G., White, T., Asfaw, B., 1991. Age of volcanism and rifting in the Burji-Soyoma area, Amaro Horst, southern Main Ethiopian rift: geo-and biochronologic data. J. Afr. Earth Sci. 13 (3–4), 437–447.
Wolela, A., 2006. Fossil fuel energy resources of Ethiopia: oil shale deposits. J. Afr. Earth Sci. 46 (3), 263–280.
Zanettin, B., Justin-Visentin, E., Massimo, N., Claudio, P., 1978. The evolution of the Chencha escarpment and the ganjuli graben (Lake Abaya) in the southern Ethiopian rift. Neues Jahrbuch Fur Geologie Und Palaontologie (8), 473–490.
Zhdanov, M.S., 2002. Geophysical Inverse Theory and Regularization Problems, 36. Elsevier.